

Radar Backscatter and Surface Roughness Measurements for Stationary Breaking Waves

Author(s): D. T. Walker, D. R. Lyzenga, E. A. Ericson and D. E. Lund

Source: *Proceedings: Mathematical, Physical and Engineering Sciences*, Vol. 452, No. 1952 (Sep. 9, 1996), pp. 1953-1984

Published by: [The Royal Society](#)

Stable URL: <http://www.jstor.org/stable/52848>

Accessed: 28/09/2013 03:17

Your use of the JSTOR archive indicates your acceptance of the Terms & Conditions of Use, available at <http://www.jstor.org/page/info/about/policies/terms.jsp>

JSTOR is a not-for-profit service that helps scholars, researchers, and students discover, use, and build upon a wide range of content in a trusted digital archive. We use information technology and tools to increase productivity and facilitate new forms of scholarship. For more information about JSTOR, please contact support@jstor.org.



The Royal Society is collaborating with JSTOR to digitize, preserve and extend access to *Proceedings: Mathematical, Physical and Engineering Sciences*.

<http://www.jstor.org>

Radar backscatter and surface roughness measurements for stationary breaking waves

BY D. T. WALKER, D. R. LYZENGA, E. A. ERICSON AND D. E. LUND

Department of Naval Architecture and Marine Engineering, University of Michigan, Ann Arbor, MI 48109-2145, USA

In this study the surface features and the radar backscatter associated with breaking waves generated by a uniform flow past a stationary submerged hydrofoil were examined. The level of energy dissipation due to breaking was varied by changing the foil angle of attack. Time series of surface elevation profiles were obtained for the breaking crest region and the following waves. Radar backscatter (X-band) was also measured for an incidence angle of 45° with the radar looking both upwave and downwave for HH and VV polarizations. These measurements were compared to model predictions of radar backscatter using the surface elevation data as inputs to the model.

The breaking crest region exhibited the largest surface disturbances, as measured by the temporal variance of the surface elevation. The maximum in the variance was associated with large low-frequency disturbances in the 'toe' region. Downstream-moving waves appear just ahead of the crest and, due primarily to interaction with the spatially varying current set up by the stationary wave, decrease in amplitude by an order of magnitude as they propagate downstream. These surface disturbances remain at a low level thereafter. A maximum radar cross-section per unit area of about 0.5 was observed near the breaking crest, for both HH and VV polarization in the upwave look direction. The maximum value for the upwave look direction was about twice as large as for the downwave look direction. Downstream of the breaking crest, the radar cross-section decreased rapidly and then leveled off, and an increasing difference between the VV and HH backscatter was observed as the overall backscatter level decreased. Near the second crest, there was a small increase in the height variance and in the radar cross-section.

The surface-elevation measurements were used as inputs for a Bragg-scattering model and the expected radar backscatter was calculated. The variations in the observed radar cross-section downstream of the breaking crest are satisfactorily explained by the Bragg model when surface-tilt effects are taken into account. However, the backscatter from the breaking crest itself is not accurately predicted since, in this region, the small-scale surface roughness exceeded the limits of validity for the Bragg model.

1. Introduction

The use of remote sensing data for observing various dynamical processes in the upper ocean hinges on the relationship between those processes and the remotely sensed variables. For the case of microwave radar remote sensing, the remotely sensed

variables are directly related to the small-scale surface roughness (on the scale of the radar wavelength). A knowledge of the relationships between this small-scale roughness, the larger-scale ocean dynamics and the radar backscatter is therefore of interest for the interpretation of radar remote sensing data.

In this study, we examine some aspects of the relationship between wave-breaking and radar backscatter. Wave breaking is a ubiquitous but poorly understood phenomenon which has implications for a number of other processes including the transfer of momentum, gases and aerosols between the atmosphere and the ocean. It also has important effects on the energy balance of surface waves and the generation of acoustic disturbances. In this study we consider stationary breaking waves generated by a stationary submerged hydrofoil in a uniform stream. The objectives were to characterize the surface roughness and radar backscatter, and to evaluate simple models which relate the two.

Increased radar backscatter from breaking waves has been previously observed in several field and laboratory experiments. Lewis & Olin (1980) associated X-band radar sea spikes at low grazing angles with breaking waves through the use of video imagery. They reported radar cross-section values on the order of 1 m^2 for individual events corresponding to breaking waves. Jessup *et al.* (1990, 1991*a, b*) found a similar association between breaking waves and backscatter spikes at intermediate (45°) incidence angles, and investigated the polarization ratio and Doppler characteristics of the backscatter spikes. Using a criterion based on both the backscattered power and the Doppler bandwidth, they found that the number of events per hour and the contribution of these events to the mean radar cross-section per unit area were both roughly proportional to the cube of the wind friction velocity, in accordance with predictions by Phillips (1988). These events were generally characterized by a radar cross-section per unit area on the order of 0.5 (as measured with a radar footprint of about 1.3 m^2) at both HH and VV polarization. Most of the larger spikes were observed on the steep forward face of near-breaking waves, and suggested that the increased backscatter was primarily due to the change in the local incidence angle.

Banner & Fooks (1985) made laboratory measurements of stationary breaking waves generated by a submerged hydrofoil in a steady stream. They found that some aspects of the microwave backscatter associated with these waves were consistent with Bragg scattering from the small-scale surface disturbances generated in the breaking zones, thus introducing a mechanism quite different from that suggested by Jessup *et al.* (1991*a*). However, because of uncertainties in the radar calibration and a lack of measurements of the small-scale roughness (Bragg wave spectral density) over the full radar footprint, Banner & Fooks (1985) were not able to quantitatively verify the Bragg hypothesis.

Melville *et al.* (1988) and Loewen & Melville (1991) conducted a set of complementary experiments involving transient breaking waves obtained by dispersive focusing of mechanically generated wave packets. Analysis of this data led to a relationship between the backscattered microwave power and the amount of mechanical energy dissipated during breaking. Although they did not make detailed measurements of the instantaneous surface profiles, they observed a large increase in backscatter just before wave breaking and suggested that this signal was due to specular reflection from the steep forward face of the waves.

Laboratory experiments involving radar backscatter from wind-generated breaking waves have also been conducted by Trizna *et al.* (1991, 1993) and Ebuchi *et al.* (1993). Using a very short pulse X-band radar operated at low grazing angles,

Trizna *et al.* observed spikes in the radar backscatter at HH polarization which they associated with the crests of short wind waves driven to extreme steepness by the passage of a longer (1.56 m) mechanically generated wave. The observed polarization characteristics of their measurements were found to be inconsistent with existing backscatter models. Ebuchi *et al.* (1993) made vv-polarization backscatter measurements at small-to-moderate ($0\text{--}45^\circ$) incidence angles using an X-band (9.6 GHz) microwave scatterometer over a range of wind speeds. They found no significant difference between the returns for breaking and non-breaking crests, as defined by the entrainment of bubbles, at a given wind speed. The apparent discrepancy between this observation and the field measurements by Jessup *et al.* (1990) was suggested by the authors to be due to qualitative differences between breaking waves in the laboratory and in the open ocean, and to the fact that in their measurements the surface roughness was so large throughout the wave tank that it obscured the contributions from the breaking waves.

In the present study we have investigated the radar backscatter from stationary breaking waves using an experimental arrangement similar to that of Banner & Fooks (1985) but with a larger flow velocity and a correspondingly longer breaking-wave length. The objectives of this study were (1) to gain insight into the nature of the small-scale surface disturbances created by wave breaking and (2) to evaluate the accuracy with which the radar backscatter can be calculated from measurements of these surface disturbances. We recognize that the breaking waves studied in these laboratory experiments are not the same as those encountered in the open ocean, and that additional mechanisms may exist in the presence of wind forcing, but experiments of this type can help to illuminate the complex hydrodynamic and electromagnetic interactions involved in the open ocean as well as in laboratory breaking waves. One advantage of this type of experiment is that the statistical stationarity of the small-scale disturbances created in this setting allows for much longer sampling intervals in both the surface measurements and the radar backscatter measurements than are possible in transient breaking waves and certainly in field experiments.

The hydrofoil-generated waves examined in this study are similar to those investigated by Duncan (1981, 1983*a*). He showed that for a breaking wave generated by a submerged hydrofoil, the forward face of the breaking wave crest has a characteristic slope of about 0.3. In addition he showed that the wavelength of the breaking wave followed the dispersion relation for finite-amplitude Stokes waves (Longuet-Higgins 1974). The results of this study exhibit similar behaviour. More recently, Duncan (1993) showed that the root-mean-square (RMS) surface-elevation fluctuations were largest near the 'toe' (most forward part) of the breaking region and decreased in the downstream direction. The fluid in the breaking region was shown by Lin & Rockwell (1994) to have nearly zero velocity relative to the wave crest.

Dissipation of wave energy by breaking is an important physical mechanism. Duncan (1983*a*) showed that drag associated with wave-breaking can be much larger than that associated with the following wave train that is generated. This indicates that there can be significant dissipation of wave energy in stationary breaking waves. Rapp & Melville (1990) examined dissipation for transient breaking waves in dispersively focused wave packets (similar to those examined in Loewen & Melville 1991). In that study, a single wave in the packet would break and 10–25% of the energy in the entire packet (typically a few wavelengths long) was dissipated. In the subsequent sections, we examine the dissipation levels for the waves investigated in the present

study and, to the extent possible, relate their behaviour to that of transient breaking waves.

In the following sections we present detailed measurements of both the surface characteristics and the radar backscatter for stationary breaking waves. Our results tend to affirm the conclusions of Banner & Fooks (1985) regarding the role of Bragg scattering, but we find that the large-scale slope also plays an important part in quantitatively explaining the observed backscatter variations, and that the Bragg model has some significant shortcomings due to the large surface height variations in the breaking region. In particular, we find that the Bragg model fails to predict the polarization ratios observed near the breaking crest for the downwave look direction. Our conclusions are based upon surface measurements made over the entire length of the radar footprint and upon calibrated radar backscatter measurements for both upwave and downwave look directions. The apparatus and procedures used to conduct this study are described in §2. The results obtained for both the hydrodynamic characteristics and electromagnetic scattering for stationary breaking waves are presented and discussed in §3, and the conclusions of the investigation are presented in §4.

2. Experimental apparatus and procedures

The experiments reported here were performed in a recirculating water channel. The breaking waves were generated by a stationary hydrofoil operating at fixed angle of attack beneath the free surface. The amount of energy dissipated by the breaking wave was controlled by varying the angle of attack of the hydrofoil. The surface elevation profiles were obtained by dyeing the water with a fluorescent dye and illuminating the surface with a laser sheet. The surface elevation data were obtained by digitally processing images captured using a monochrome CCD camera. Velocity and total-pressure surveys were done using a pitot-static probe. Microwave backscatter measurements were made using a 10.5 GHz Doppler radar looking both upwave and downwave at a 45° incidence angle.

(a) *Water channel*

(i) *Description of water channel*

The free-surface water channel used for this investigation is shown in figure 1. The channel resides on two floors in the University of Michigan's Marine Hydrodynamics Laboratory. The channel was designed using an approach similar to that which is typically used in the design of wind tunnels, and relied heavily on the methodology outlined by Bradshaw & Pankhurst (1964). It is constructed entirely of 0.013 m thick PVC plastic supported by a steel frame enclosure. The water channel holds approximately 8000 gallons of water. Water for the channel is first carbon filtered to remove any oils or other organic contaminants, then softened, and finally filtered to remove particulates down to 1 µm.

The water channel is driven by a 0.787 m diameter four-bladed bronze impeller attached to a 20 hp three-phase induction motor through a 6:1 reduction gear. The impeller was constructed by cutting down a 0.813 m diameter 0.686 m pitch, pleasure-boat propeller (a Dyna-Quad propeller from Michigan Wheel Corp., Grand Rapids, MI). (The diameter was reduced to create a broader blade tip, and minimize the tip clearance flow.) The propeller shaft is stainless steel, and is supported by a water-lubricated bronze journal riding in a stainless steel bearing just downstream of the

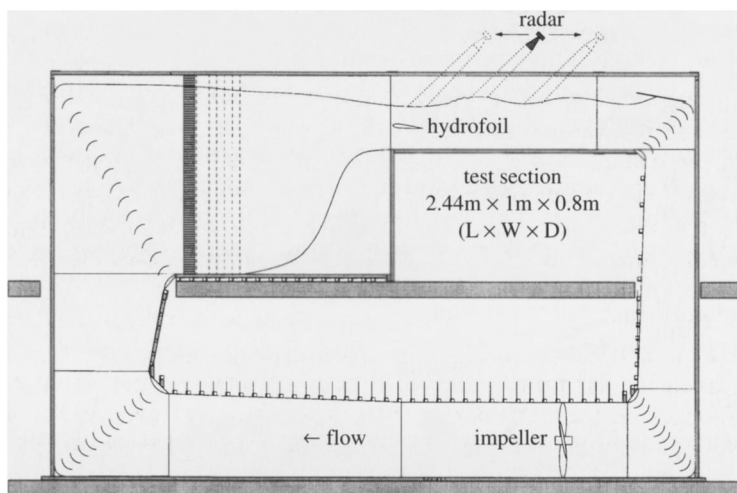


Figure 1. Schematic of water channel showing the hydrofoil and breaking wave; radar is shown oriented for downwave backscatter measurements.

impeller. The other end of the propeller shaft is supported by the reduction gear through a rigid coupling. The propeller shaft is sealed, where it passes through the channel wall, by a neoprene rubber seal. The speed of the drive motor is controlled by a variable frequency three-phase drive, and is 1750 RPM at a frequency of 60 Hz. Operation with a nominally 1 m s^{-1} velocity in the test section requires the motor to be driven at 27 Hz, or 787 RPM; this results in a propeller rotation rate of 131 RPM.

The test section is constructed of 0.0254 m thick clear acrylic to allow good optical access from all directions. The test section is 1.00 m wide by 2.44 m long, and the water depth can be up to 0.8 m. The maximum water velocity is 2 m s^{-1} and is attained in the test section. Downstream of the test section, the flow turns downward and passes through to the lower level. After the impeller, a gradual increase in section area begins which is carried through two more right-angle turns before reaching the settling chamber upstream of the test section. At each corner of the channel, stainless steel turning vanes accomplish the required right-angle turn without generating undesirable large-scale secondary flows.

In the settling chamber upstream of the test section, a honeycomb flow straightener, screens and an area contraction result in a uniform low-turbulence flow in the test section. The flow first passes through a honeycomb section immediately followed by a screen, as recommended by Loehrke & Nagib (1972). The honeycomb section consists of 0.00635 m diameter thin-wall plastic (polyetherimide) tubes which are 0.010 m long and are bonded in a hexagonal closest-packed array. This material was manufactured by Plascore Inc. (Zeeland, MI). This section functions as a flow straightener and removes any large-scale vorticity from the flow. The honeycomb is immediately followed by a stainless steel (type 304) screen with a wire diameter of $d = 0.203 \text{ mm}$ and spacing of 1.41 mm. (This results in an open-area ratio of 73% for the screen.) Five similar screens are located starting 0.20 m downstream of the honeycomb section and are spaced 0.10 m (approximately $500d$) apart. The spacing between the screens was chosen so that the turbulence generated by each screen would decay to a low level before the flow reached the next, based on the recommendations by Loehrke & Nagib (1972) and Bradshaw & Pankhurst (1964). The contraction is two dimensional (only the depth of the flow changes, not the

width) and has a 4:1 area ratio. It was designed using the methodology outlined by Whitehead *et al.* (1951). This approach results in the minimum amount of adverse pressure gradient in the boundary layer at the beginning and end of the contraction.

As shown by Whitehead *et al.* (1951), truly uniform flow can only be attained using a contraction of infinite length. Due to space restrictions, which imposed a limitation on the physical size of the water channel, the contraction was constrained to be roughly 1.3 m in length. This resulted in a roughly 10% velocity excess near the floor of the test section. To make the flow more uniform in the test section, screens which spanned the lower portion of the settling chamber upstream of the contraction were used to introduce a momentum deficit in the lower portion of the flow arriving at the contraction. This resulted in a more uniform flow over the channel cross-section.

(ii) *Qualification tests*

Pitot tube surveys of the streamwise velocity were done to establish the uniformity of the flow, and hot-film anemometer measurements were used to determine the turbulence level. These measurements were done at a flow velocity of 1.1 m s^{-1} in the test section, similar to the velocity used in the measurements of breaking waves. The streamwise velocity is uniform to within 1.4% RMS over the entire cross-sectional area of the test section. For the upper two-thirds of the test section, the region of interest for the flows examined here, the flow is uniform to within 0.4% RMS.

Turbulence levels were quantified using a TSI Inc. (Minneapolis, MN) Model 1054A constant temperature anemometer with a TSI Model 1260A-10W cylindrical hot film probe. The output of the anemometer was not linearized, and the system was calibrated over a small range of velocities near 1.1 m s^{-1} . The bridge output from the anemometer was digitized and the RMS velocity fluctuation level was calculated. A cylindrical hot film responds to two components of the fluctuating velocity, and so captures two-thirds of the turbulence kinetic energy (assuming that the turbulence is isotropic). This was used to determine the turbulence kinetic energy level k . The square-root of k normalized with the free stream velocity is 0.000 95, and so the turbulence level for the channel is 0.095%.

(iii) *Hydrofoil*

The hydrofoil used to generate the stationary breaking waves has a symmetric section. The chord is 0.304 m and the thickness is 15% (NACA 0015). The angle of attack α was varied to increase the steepness of the resulting wave. The angle of attack could be varied over the range $-10^\circ < \alpha < 10^\circ$, by pivoting the foil about its quarter-chord location. This is approximately the range of unstalled operation for this foil section. The waves observed in this study were generated with $0^\circ < \alpha < 6^\circ$. For $\alpha = 0$, a steep non-breaking wave was generated. For $\alpha \geq 3^\circ$, breaking waves were generated; the results for the specific angles of 3, 4 and 6° are presented later. The pivot point is located 0.330 m above the channel bottom at a distance of 0.50 m downstream of the test section inlet and it is 0.267 m below the undisturbed free surface.

(b) *Surface-elevation measurements*

(i) *Optical set-up*

The surface elevation was determined using a method first introduced by Duncan (1981) in a study of similar hydrofoil-generated breaking waves. In this approach the water is dyed using a fluorescent dye. A sheet of laser light is then brought vertically

downward to the free surface from above. Where the light sheet intersects the free surface, the dye fluoresces and, if viewed from a direction normal to the light sheet, the fluorescent emission defines the surface-elevation profile.

For the waves examined here, the dye used was Fluorescein disodium salt, in a concentration of a few parts per million. The surface was illuminated with a laser sheet generated using a Liconix Corp. 4 W argon-ion laser operating with a multiline output of approximately 5 W. The laser beam was formed into a sheet approximately 1 mm thick and 0.50 m wide using a combination of spherical and cylindrical optics. The optics were arranged so that the final stage of the optics was located on a carriage which moved along the length of the test section. In this way the laser sheet could be placed at any position from ahead of the breaking wave crest, to the crest of the second following wave. The fluorescent emission was captured with an RS170-format CCD camera with a framing rate of 30 Hz. To 'freeze' the images the laser sheet was strobed once per frame (with an exposure time of 2 ms) using an acousto-optical modulator from Newport Electro-Optical Systems (Melbourne, FL).

The images were captured using a Cohu, Inc. (San Diego, CA) Model 4915/ER2225 monochrome CCD camera. This camera was modified to provide a variable-duration output TTL pulse to control the acousto-optical modulator which strobed the laser sheet. Because of the highly three-dimensional nature of the water surface, the camera was mounted so as to look downward at 45° , so that the intersection of the laser sheet with the water surface was not obscured by disturbances in the foreground. A 25–90 mm $f/1.8$ lens was used with the focal length set to result in a field of view 0.405 m wide at the water surface. The orientation of the camera results in a distorted image in the plane of the laser sheet, due to perspective. The spatial locations in the plane of the laser sheet were determined using a calibration grid, with 2.5 mm spacing of the grid lines in the horizontal and vertical directions. Images of this grid were used to relate the individual pixels of the CCD array to spatial locations in the plane of the laser sheet. This allowed positions to be determined to roughly 0.8 mm in the horizontal and vertical directions.

Images were acquired for five streamwise regions, each 0.405 m long. The images spanned the region from the trough upstream of the breaking crest to the second crest following the breaking wave. Each of the five sets of images overlapped the adjacent sets by 1–2 cm so that no gaps existed in the data. Image sequences were captured in real time using a Perceptics, Inc. (Knoxville, TN) digitizer with a resolution of 512×480 pixels operating in a Macintosh II/fx computer. A 32 MB buffer allows the capture of up to 128 sequential images at the camera's framing rate. For the work presented below, two sequences of 128 frames each, a total of 256 images, were acquired for each streamwise region; 1280 images for each of the three breaking wave conditions examined. The data were stored on a 1.4 GB hard disk before and during processing, and were then archived to 8 mm DAT tape.

(ii) *Data analysis*

The digitized images of the intersection of the laser light sheet with the free surface were analysed to extract information on the surface elevation. This information consisted of a time-history of the surface elevation profiles for a given 0.405 m long region. The data were processed in three stages. First, the pixel locations for the line corresponding to the dark-to-bright transition (which corresponds to the location of the free surface) were determined. This was done by identifying the uppermost local maximum in the vertical component of the intensity gradient for a given pixel col-

umn. This location was determined subject to a continuity constraint which assumed that the surface elevation could change no more than a specified number of pixels from one streamwise position to the next. In practice, the continuity condition was required to minimize the effects of spray and droplets which were detached from the surface. The continuity condition was set to allow a maximum slope of 10 pixels per pixel. Next the calibration data were used to determine the absolute spatial coordinates corresponding to the pixel values. Because of the distortion in the images (caused by the 45° viewing angle), and the varying surface elevation, the exact x positions for the surface elevation data in a pixel column vary from frame to frame. Therefore, the final step in processing was to interpolate the data onto a regular grid of 512 spatial locations, using linear interpolation. These data were then used to calculate the mean and RMS surface elevation profiles, wavenumber and frequency spectra and covariance functions.

Due to large local steepness or significant three dimensionality of the surface in the breaking region, occasionally the detection of the free-surface position would fail. In these cases, no data was recorded for the free surface elevation for a given streamwise location. In the calculation of the statistics, the ensemble size was therefore slightly reduced. For the calculation of spectra and correlations, incomplete data cannot be tolerated, and the voids were filled by linear interpolation. The occurrence of these 'drop-outs' was most pronounced in the breaking region, where large free-surface disturbances occur, and more likely in the more violently breaking waves. Typically only a few dropouts would occur in a given 512-element surface elevation profile.

An additional statistical test was applied at each spatial location to identify questionable data. After calculating the temporal mean and standard deviation, all data points more than three standard deviations from the mean were eliminated. This resulted in the removal of a few data points, as would be expected from Gaussian statistics.

(c) *Radar backscatter measurements*

Radar backscatter measurements were made at an incidence angle of 45° in both the upwave and downwave directions, using the X-band Doppler radar instrumentation described below. Measurements were made with both vertical and horizontal polarization by physically rotating the antenna about its axis, and the measurements were repeated at 0.10 m intervals in the along-tank direction by moving the radar along a track on the top of the water channel. Data analysis procedures are described in § 2 c (iii) and results are presented in § 3 b.

(i) *Radar instrumentation*

The radar instrumentation used in this study was constructed from a low-cost commercially available microwave transceiver (M/A-COM model MA86735) attached to a standard-gain horn antenna (Scientific Atlanta model 12-8.2). The transceiver consists of a Gunn diode oscillator operating at 10.525 GHz, along with a pair of Schottky diode mixers mounted in a small section of waveguide so as to detect the coherent sum of the outgoing (transmitted) and incoming (received) fields. The spacing of the detectors is chosen to sample the in-phase and quadrature components of the resultant field. Thus, a single scatterer moving at a constant radial velocity would produce a sinusoidal output signal at each of the detectors with a nominal phase difference of 90° between the two signals.

The radar was mounted on a frame which allowed the system to be translated

along the top of the water channel, with the centre of the antenna aperture located 0.72 m above the mean water surface. Radar absorbing material was placed above the water surface so as to allow only the main lobe of the antenna pattern to illuminate the water surface and to prevent the forward-scattered radiation from being reflected back into the field of view by other objects in the room.

(ii) *Radar calibration*

Under the ‘spatial-whiteness’ hypothesis (Hasselmann *et al.* 1985), the backscattered power from the water surface can be expressed as

$$P_r = P_t \lambda^2 \iint \frac{G^2(\theta, \phi)}{(4\pi)^3 r^4} \sigma^0(x, y) dx dy, \quad (2.1)$$

where P_t is the transmitted power, λ is the radar wavelength, $G(\theta, \phi)$ is the one-way antenna gain, r is the distance from the antenna to the point (x, y) on the surface and $\sigma^0(x, y)$ is the radar cross-section per unit area of the water surface. If σ^0 is assumed to be constant over the illuminated area, this equation can be rewritten as

$$P_r = P_t \frac{\lambda^2 G_0^2 A_i}{(4\pi)^3 r_0^4} \sigma^0, \quad (2.2)$$

where

$$A_i = \frac{r_0^4}{G_0^2} \iint \frac{G^2(\theta, \phi)}{r^4} dx dy \quad (2.3)$$

is the illuminated area, r_0 is the range distance to the centre of the illuminated area and G_0 is the peak or boresight antenna gain.

In order to calculate the radar cross-section per unit area σ^0 , we compared the backscattered power from the water surface with the power received from a point target of known cross-section σ_c located in the centre of the antenna beam at a range distance r_c . This calibration power can be expressed as

$$P_c = P_t \frac{\lambda^2 G_c^2}{(4\pi)^3 r_c^4} \sigma_c, \quad (2.4)$$

where G_c is the antenna gain at the target location. Thus, the ratio of the backscattered power from the water surface to the calibration power is

$$\frac{P_r}{P_c} = \left(\frac{G_0}{G_c}\right)^2 \left(\frac{r_c}{r_0}\right)^4 \left(\frac{A_i}{\sigma_c}\right) \sigma^0, \quad (2.5)$$

which can be readily solved for σ^0 if the illuminated area A_i is known. Calibration measurements were made using a 0.15 m diameter aluminum sphere at $r_c = r_0 = 1$ m, so our calibration equation reduces to

$$\sigma^0 = \left(\frac{\sigma_c}{A_i}\right) \frac{P_r}{P_c}, \quad (2.6)$$

where $\sigma_c = 0.0177$ m².

To obtain the illuminated area, the electric and magnetic fields at the aperture of the horn antenna were assumed to have an amplitude weighting as in the TE₁₀ waveguide mode and a quadratic phase variation as described in Balanis (1982, ch. 12). These fields were substituted into the Stratton–Chu equations in order to calculate the incident field on the water surface. Because of the relatively short ranges

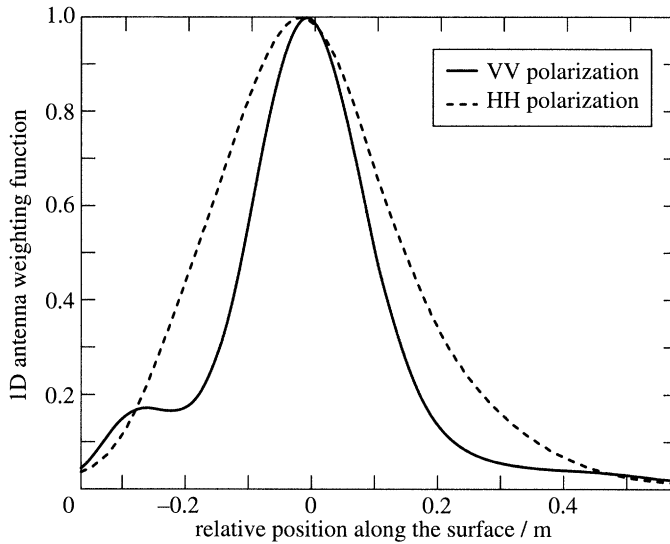


Figure 2. Spanwise-integrated radar antenna pattern for HH and VV polarization, and 45° incidence angle.

involved in the experiment, no far-field approximations were made in calculating the incident field. Equation (2.3) was numerically integrated over the main lobe of the antenna pattern, yielding $A_i = 0.066 \text{ m}^2$. Integrating this equation in the cross-channel direction yields the streamwise weighting function

$$A_i(x) = \frac{r_0^4}{G_0^2} \int \frac{G^2(\theta, \phi)}{r^4} dy, \quad (2.7)$$

which is plotted for both antenna polarizations in figure 2. Note that the half-power width of this weighting function in the streamwise direction is approximately 21 cm for VV polarization and 33 cm for HH polarization. In the cross-channel direction, the illuminated area was well within the width of the channel.

(iii) Data acquisition and analysis

The output signals from each of the detectors were sampled at a rate of 512 samples per second using a Metrabyte DAS-8 A/D board installed in an Intel 486-based computer. A bias signal, which is typically on the order of 0.5 V, was removed from each of the two output signals using a blocking capacitor and the fluctuating component was amplified by a factor of approximately 200 before A/D conversion. Data were recorded for a period of 32 s for each location and polarization.

During processing, the recorded voltages v_1 and v_2 from the two detectors were scaled so as to equalize their variances and these scaled values were assigned to the real and imaginary parts of a complex variable s_n . 1 s averages of the received power were then calculated as

$$P_r = \frac{1}{N} \sum_{n=1}^N |s_n|^2, \quad (2.8)$$

where $N = 512$, and 32 of these 1 s power measurements were further averaged together and converted into estimates of the radar cross-section per unit area using the calibration procedure described previously.

3. Results

Breaking waves for a constant flow velocity and three different angles of attack were examined. The three angles of attack caused differing amounts of dissipation to occur as a result of the wave breaking. In what follows, first the overall behaviour of the breaking waves is presented by examining the wavelength, amplitude, steepness, dissipation levels, etc. Profiles of the instantaneous and mean surface elevation are then presented along with profiles of the variance of the surface elevation. Representative behaviour of the crest region of one of the waves is examined using wavenumber–frequency spectra and related quantities. Radar backscatter measurements are then presented and compared to predictions obtained using the Bragg-scattering model.

(a) Overall behaviour of the breaking waves

The flow velocity U_0 , measured at the inlet plane of the test section, ranged from 1.07–1.10 m s⁻¹. Based on linear theory, a flow velocity of 1.08 m s⁻¹ would result in a gravity wave with a length of 0.75 m. The observed wavelengths ranged from 0.72–0.73 for the breaking waves and 0.68–0.75 m for the first wave following the breaking waves. The amplitudes of these following waves were such that the residual wave steepness was $ak = 0.09$ – 0.18 . The exact values of these parameters varied from one case to the next and are summarized in table 1. Also included in the table for comparison are data for a steep non-breaking wave generated with the hydrofoil set at a zero degree angle of attack.

The amplitude and wavelength associated with the breaking-wave crest region, a_b and λ_b , respectively, are shown in table 1, along with the associated steepness $(ak)_b$, where $k = 2\pi/\lambda$ is the wavenumber. (These data were obtained from the laser-induced fluorescence surface elevation measurements; the complete surface elevation profiles are presented in § 3 c.) Following Duncan (1981), the amplitude a_b is defined as half the vertical distance from minimum mean surface elevation in the trough ahead of the breaking crest to the maximum mean surface elevation in the crest region. The wavelength is the horizontal distance from the minimum mean surface elevation in the trough ahead of the breaking crest to the minimum mean surface elevation in the trough behind. The wave steepness $(ak)_b$ is calculated from these two numbers. For the breaking waves, $\alpha \neq 0$, the resulting steepness is at roughly 0.32 ± 0.03 . This is comparable to the angle of 17° (slope of 0.31) obtained by Duncan (1983a) and is apparently a ‘universal’ characteristic of stationary breaking waves. For waves of this steepness, the appropriate dispersion relation for the phase velocity is $c = 1.053(g/k)^{1/2}$ (Duncan 1983b). The calculated phase velocities are presented in table 1 and are seen to agree with the measured value of U_0 to within 4%. These results for the breaking wave crest are similar to those in Duncan (1981, 1983a).

Data for the waves which follow the breaking crest are also contained in table 1. The wavelength of the following waves (λ) is the horizontal distance measured from the point of minimum mean surface elevation in the first trough after the breaking crest region to the same point in the second trough. The amplitude is half the vertical distance from the crest to the trough. For the breaking waves, the amplitude of the following waves decreases with increasing angle of attack. The wavelength also decreases, with the waves for $\alpha = 3^\circ$ and 4° being about 8% shorter than the non-breaking wave at $\alpha = 0^\circ$ and the strongly breaking wave ($\alpha = 6^\circ$) being 15% shorter. The steepness of the following wave trains in the breaking wave cases vary, with the largest angle of attack having the smallest steepness, and vice versa. This is indicative

Table 1. *Parameters for the waves examined in this study*

angle of attack α	0°	3°	4°	6°	uncertainty
free-stream velocity U_0 (m/s)	1.07	1.08	1.10	1.08	0.020
Breaking wave crest					
wavelength λ_b (m)	0.794	0.722	0.719	0.726	0.007
wavenumber k_b (rad m ⁻¹)	7.91	8.70	8.74	8.65	0.079
amplitude a_b (m)	0.024	0.038	0.037	0.037	0.001
steepness ak_b	0.186	0.326	0.319	0.320	0.030
C (from equation (3.5))	1.152	1.175	1.167	1.174	0.012
Following wave crest					
wavelength λ (m)	0.805	0.743	0.751	0.684	0.007
amplitude a (m)	0.026	0.026	0.018	0.010	0.001
wavenumber k (rad m ⁻¹)	7.810	8.457	8.363	9.185	0.079
steepness ak	0.200	0.218	0.154	0.092	0.030
phase velocity C (m s ⁻¹)	1.166	1.128	1.109	1.042	0.012
$C/(g/k)^{1/2}$	1.040	1.047	1.024	1.008	0.010
Power estimates					
dissipation (W m ⁻¹)	0.07	2.96	3.78	8.85	0.39
following wave power (W m ⁻¹)	1.89	1.84	0.93	0.26	0.45
total wave power (W m ⁻¹)	1.96	4.80	4.71	9.11	0.59
estimated dissipation (%)	4	62	80	97	—
(range %)	(-16-24%)	(50-73%)	(67-93%)	(90-105%)	
equivalent prebreaking steepness $(ak)^f$	—	0.33-0.39	0.33-0.39	0.44-	—

of the larger amounts of dissipation which occur in the more violently breaking waves resulting from the larger angles of attack.

(b) Dissipation

Also shown in table 1 are estimates of the work rate required to move the foil at the speed indicated. These values were based on the estimated dissipation rate for the wave breaking, and the estimated energy flux associated with the residual following wave train. The former was determined from measured total-pressure and velocity profiles obtained upstream and downstream of the breaking region, and the latter from third-order theory (Duncan 1983*b*), using the measured wavenumber and wave steepness of the residual wave train.

The dissipation rate associated with wave breaking for the case examined here can be determined using a control-volume analysis. The control volume used in this analysis has the free surface as its upper boundary and a streamline located well below the breaking region, but well above the wake of the hydrofoil, as its lower boundary. (There must be no shear stress at any location along this streamline.) The upstream boundary is a vertical plane, transverse to the flow, located in the undisturbed flow upstream of the hydrofoil. The downstream boundary can be any vertical plane downstream of the breaking region. For this control volume there is no

work done on the system by the surroundings and the dissipation rate is equal to the net flux of energy through the upstream and downstream boundaries. Conservation of energy for this situation is then written as

$$\dot{E}_b = - \int_S P(\mathbf{V} \cdot \mathbf{n}) dS, \quad (3.1)$$

where \dot{E}_b is the dissipation rate associated with wave breaking, P is the total pressure, S is the control surface, \mathbf{V} is the fluid velocity and \mathbf{n} is the outward-pointing unit surface normal. The total pressure is given by $P = p + \frac{1}{2}\mathbf{V} \cdot \mathbf{V} + \rho gz$, where p is the static pressure, ρ is the fluid density, g is the acceleration due to gravity and z is elevation measured relative to a fixed reference. Evaluating the integral at the upstream and downstream boundaries yields the following for dissipation rate (per unit width):

$$\dot{E}'_b = \int_{z_0}^{\eta_0} P_0 U_0 dz - \int_z^{\eta} P(z')u(z') dz' = P_0 U_0(\eta_0 - z_0) - \int_z^{\eta} P(z')u(z') dz', \quad (3.2)$$

where η is the water surface elevation and z is the local elevation of the streamline which constitutes the lower boundary of the control volume; the zero subscript denotes quantities evaluated at the upstream boundary, and no subscript corresponds to the downstream boundary. Applying the continuity equation to the same control volume yields

$$U_0(\eta_0 - z_0) = \int_z^{\eta} u(z') dz'. \quad (3.3)$$

Combining this with (3.2) results in

$$\dot{E}'_b = P_0 \int_z^{\eta} u(z') dz' - \int_z^{\eta} P(z')u(z') dz' = \int_z^{\eta} (P_0 - P(z'))u(z') dz', \quad (3.4)$$

and so the dissipation due to breaking can be determined from the reduction in total pressure from the upstream to the downstream boundaries of the control volume. The lower limit for the integration in (3.4) is any location between the wake of the breaking wave and the wake of the hydrofoil. In practice, the appropriate location for the lower boundary was located by examining the total pressure profiles. In the irrotational flow between the two wakes, the total pressure equaled that in the oncoming flow; in the wake regions, the total pressure was substantially reduced. The integration was carried out using total pressure and velocity measurements obtained from a pitot-static tube traversed vertically at the location of the second following wave crest.

The rate of energy flux associated with the following wave train was estimated using third-order Stokes wave theory (Duncan 1983*b*) as

$$\dot{E}'_w = \frac{1}{4}(\rho C^5/4g)a^2 k^2(1 - \frac{7}{2}a^2 k^2), \quad (3.5)$$

where $C = (g/k)^{1/2}(1 + a^2 k^2)$. The sum of the result from (3.5) and the estimated dissipation from (3.4) is the total power input into the wave system created by the hydrofoil \dot{E}' . The fractional dissipation is then \dot{E}'_b/\dot{E}' .

The resulting measurements are presented in table 1. The 95%-confidence-interval uncertainty is estimated at 0.39 W m⁻¹ for \dot{E}'_b , 0.45 W m⁻¹ for \dot{E}'_w and 0.59 W m⁻¹ for \dot{E}' . For the non-breaking wave, \dot{E}'_b is estimated at 0.07 W m⁻¹—essentially zero dissipation, as would be expected. The dissipation increases monotonically with increasing angle of attack, reflecting the increased violence of the wave breaking. The

following wave power \dot{E}'_w decreases monotonically as the angle of attack increases for the breaking wave, with a six-fold change over the range of breaking waves. The total wave power \dot{E}' is essentially the same for $\alpha = 3^\circ$ and 4° ; the increase in angle of attack increases the violence of the breaking, and the attendant dissipation, but results in no increase in the total power input. The fractional dissipation increases monotonically with increasing angle of attack, ranging from 62% at $\alpha = 3^\circ$ to 97% at 6° .

The levels of dissipation are surprisingly large for all the waves examined; however, they are comparable to those obtained by Duncan (1983*a*). The case for $\alpha = 3^\circ$ appears under casual observation to be a relatively gentle breaker, with a small amount of air entrainment. The breaking region extends forward from the crest a distance of about 12–15% of the wavelength, which is consistent with the behaviour of transient spilling breakers. Rapp & Melville (1990) examined transient spilling breakers resulting from dispersively focused wave groups and saw dissipation levels ranging from 10–25% for spilling and plunging deep-water breaking waves. The largest dissipation levels occurred for plunging breakers which resulted from wave groups which focused in such a way as to result in steepnesses (in the absence of breaking) of $0.3 < ak < 0.5$ (ak_c in Rapp & Melville's nomenclature). In this range of steepnesses, the dissipation was 20–30%. The number of wavelengths in the various groups ranged roughly from one to five.

For comparison to Rapp & Melville's ak_c , we can use the total power estimates and third-order theory to determine the equivalent prebreaking wave steepness $(ak)'$ using (3.5) with \dot{E}' and k as inputs. This is, in a sense, similar to the ak_c quantity used in Rapp & Melville (1990). For the case with $\alpha = 3^\circ$ the wave has an equivalent prebreaking steepness of $(ak)' \approx 0.36$. For this steepness, Rapp & Melville (1990) observed roughly 25% dissipation for wave groups 2.8 wavelengths long. In these groups, only a single wave would break (as a plunging breaker) but the dissipation levels were calculated for the group, not for an individual wave in the group. Hence, the dissipation level for the case with $\alpha = 3^\circ$ (62%) is two to three times the level observed by Rapp & Melville for a similar steepness wave group containing 2.8 waves, of which only one is breaking. Considering the length of the wave group examined by Rapp & Melville, the dissipation levels observed for the 3° case are not unreasonable. The 4° angle of attack case has the same prebreaking steepness as the case for 3° , but a third more dissipation. This difference is not inconsistent with the variation shown by Rapp & Melville (1990) for this range of steepnesses.

The 6° angle of attack case exhibits a significantly higher level of prebreaking steepness—larger than the limiting steepness of 0.44 for gravity waves—and tremendous dissipation (97%). In this wave, the breaking region extends forward almost to the trough ahead of the breaking crest; this is a significantly larger breaking region than is seen in transient breakers. The dissipation levels observed here are probably beyond the range of those attainable in transient breakers.

A few additional comments about transient versus stationary breaking waves are in order. First, in transient breaking waves, such as those examined by Rapp & Melville (1990), the steepness of the waves is varied in time by dispersive focusing of the wave group. This focusing causes the steepness of the group to first increase, and then to decrease. Since 'breaking' requires some time to develop, the rapid increase and then decrease of the wave steepness may not allow the breaking process to evolve fully. When the waves are steepened by a gradual and sustained increase in steepness, the breaking events may be more closely related to those of the stationary

breaking waves. This was demonstrated by the results of Ramberg & Griffin (1987), which showed that for waves in a slightly convergent channel, where the breaking is sustained over a longer period, the rates of energy loss were nearly twice those of Melville & Rapp (1985) for plunging and spilling breakers. (The results of Melville & Rapp (1985) are comparable to those of Rapp & Melville (1990).) Second, for the prebreaking steepnesses $(ak)'$ examined here, the results of Rapp & Melville (1990) show the occurrence of plunging breakers. This may be due to the rate at which the steepness increases in their study, or it may be a more universal behaviour. For the stationary waves examined in the present study, the breakers would all be classified as spilling breakers. For the stationary case to result in a plunging breaker, the cavity which forms between the crest and the impinging jet would have to be maintained indefinitely. Since even in the case of a transient breaker this cavity collapses eventually, it is unlikely that the stationary breaker will ever resemble a plunging breaker. However, the behaviour of the plunging breaking wave after the cavity collapses may be similar to that of the stationary breaker.

(c) *Surface elevation measurements*

(i) *Statistical quantities*

Figures 3–5 show a summary of the basic hydrodynamic and radar backscatter results for the three angles of attack which result in breaking waves. The results are plotted against streamwise position, in laboratory coordinates. The entrance to the test section is located at $x = 0.27$ m and the foil leading edge is located at $x = 0.42$ m. The flow is from left to right and so the wave is effectively propagating from right to left. In each of the figures, (a), (b) and (c) show the instantaneous surface elevation η , the mean surface elevation $\bar{\eta}$ together with the mean slope $\bar{\eta}_x$ and the variance of the surface elevation

$$\eta'^2 = \overline{(\eta - \bar{\eta})^2}, \quad (3.6)$$

respectively. Here, the overbar indicates a temporal average at a given streamwise (x) location. The results are presented for five overlapping streamwise regions, each 0.405 m in length; this corresponds to the field of view of the CCD camera used to acquire the images from which the surface elevation profiles were obtained. The region investigated spans about 2 m, or roughly 2.5 wavelengths of the underlying wave.

Figure 3 shows the results for the case with an angle of attack of 3° . This resulted in the minimum level of dissipation for the cases examined. Figure 3a shows samples of the instantaneous surface-elevation profiles for the five streamwise regions. The data are shown in dimensional form with the origin of the vertical coordinate at the pivot point for the hydrofoil. The scale for the vertical axis is the same as the horizontal axis and so the surface elevation profiles are undistorted and are not exaggerated. The breaking wave crest is clearly shown centred near $x = 1.1$ m, a little more than half a wavelength aft of the foil. The smooth surface upstream of the breaking region is clearly evident, as is the beginning of the breaking region. The region of strong surface activity begins about 0.11 m ahead of the wave crest (15% of the wavelength) and extends a similar distance downstream of the crest. Some roughness is evident after this region, but it is at significantly lower level. Figure 3b shows the temporal-mean surface-elevation and surface-slope profiles for this case. The beginning of the breaking region is identified in these profiles as the somewhat abrupt change in slope on the forward face of the breaker, and the maximum slope

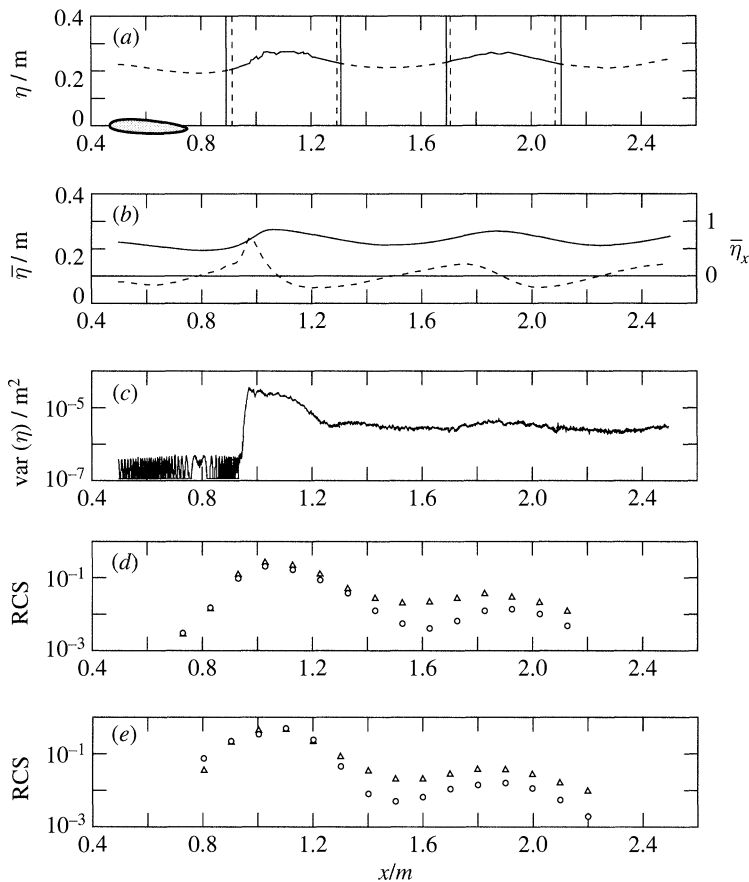


Figure 3. Summary of results for the breaking wave for $\alpha = 3^\circ$. (a) Examples of instantaneous surface-elevation profiles for the five streamwise regions. (b) Temporal mean profiles of: —, surface elevation $\bar{\eta}$; - - -, surface slope $\bar{\eta}_x$. (c) Surface elevation variance. Radar cross-section measurements for: (d) downwave look direction; (e) upwave look direction; \circ , HH polarization; \triangle , VV polarization.

is roughly twice the wave steepness ak . Figure 3c shows the variance of the surface elevation for the five streamwise regions. Ahead of the breaking region, the variance is relatively constant at $4.4 \times 10^{-7} \text{ m}^2$. In this region the water level is constant and so the variance is actually a measurement of the noise level for the surface elevation measurements. This indicates that the RMS error in the displacement measurements is about 0.7 mm, comparable to the resolution of the video images. The maximum variance $3.1 \times 10^{-5} \text{ m}^2$ occurs near the ‘toe’ of the breaking wave and is associated with the fore-and-aft surging of the breaking region. This was also observed by Duncan (1993) in similar waves. The variance decreases monotonically downstream to a level of $2.0 \times 10^{-6} \text{ m}^2$ for distances larger than 0.18 m downstream of the breaking crest (24% of the wavelength). (This rapid fall-off in the variance of the surface elevation is investigated below by examining the wavenumber–frequency spectra in the breaking crest region.) Downstream of the breaking region, there is a small-amplitude undulation in the level of the variance—a slight increase near the second crest and decreases in the troughs. This is due to the interaction of the short-wave disturbances with the orbital velocities of the underlying steady wave.

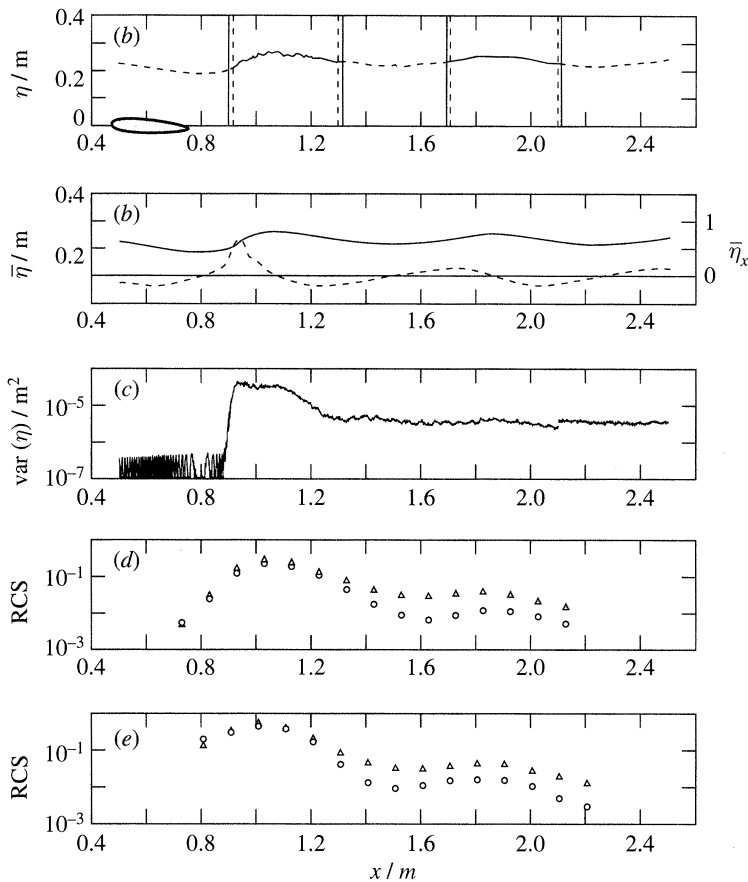


Figure 4. Summary of results for the breaking wave for $\alpha = 4^\circ$. (a) Examples of instantaneous surface-elevation profiles for the five streamwise regions. (b) Temporal mean profiles of: —, surface elevation $\bar{\eta}$; - - -, surface slope $\bar{\eta}_x$. (c) Surface elevation variance. Radar cross-section measurements for: (d) downwave look direction; (e) upwave look direction; \circ , HH polarization; Δ , VV polarization.

Figure 4 shows the results for the case with an angle of attack of 4° . This resulted in the intermediate level of dissipation for the cases examined (80%). Figure 4a shows samples of the instantaneous surface elevation profiles for the five streamwise regions. The breaking wave crest has moved slightly forward, to $x = 1.07$ m, but the region of strong surface activity now begins about 0.13 m ahead of the wave crest (nearly 19% of the wavelength) and, again, extends a similar distance downstream of the crest. Figure 4b shows profiles of the temporal mean of the surface elevation and slope for this case. Again, the beginning of the breaking region is identified in these profiles as an abrupt change in slope on the forward face of the breaker, with a maximum slope of about $2ak$. The amplitude of the following wave is about 30% smaller than for the case with $\alpha = 3^\circ$. This is due to the increased level of dissipation discussed above. Figure 4c shows the variance of the surface elevation for the five streamwise regions. Ahead of the breaking region, the variance is at the noise level for the surface elevation measurements. The maximum variance, $4.4 \times 10^{-5} m^2$, again occurs near the 'toe' of the breaking wave. The variance decreases rapidly downstream to a level of $3.5 \times 10^{-6} m^2$ for distances larger than 0.23 m downstream of the breaking

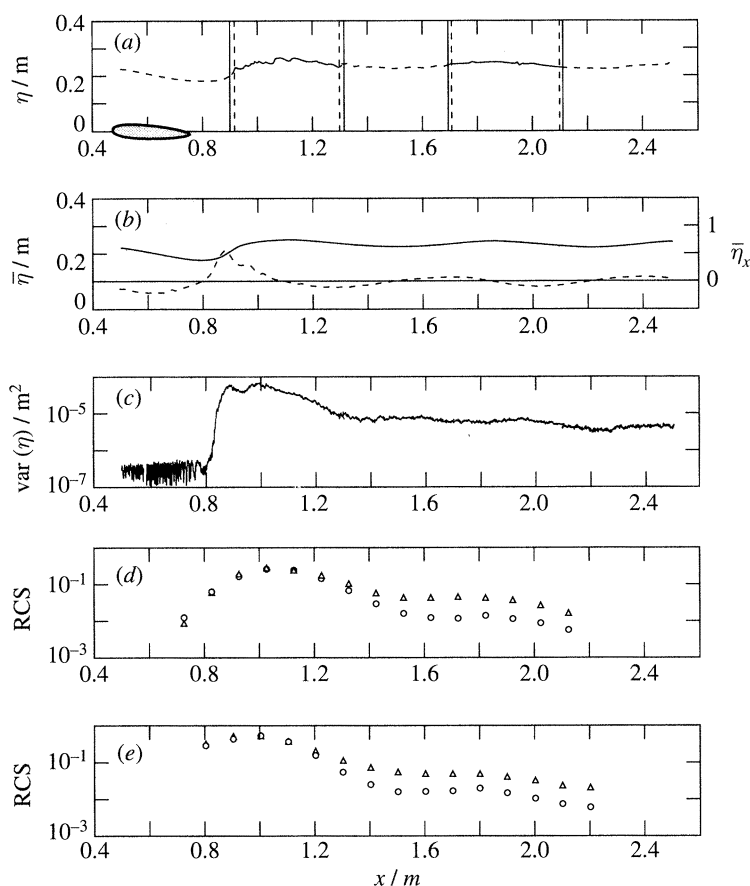


Figure 5. Summary of results for the breaking wave for $\alpha = 6^\circ$. (a) Examples of instantaneous surface-elevation profiles for the five streamwise regions. (b) Temporal mean profiles of: —, surface elevation $\bar{\eta}$; - - -; surface slope $\bar{\eta}_x$. (c) Surface elevation variance. Radar cross-section measurements for: (d) downwave look direction; (e) upwave look direction; \circ , HH polarization; \triangle , VV polarization.

crest (30% of the following wavelength). Downstream of the breaking region, there is again a slight increase in the variance near the second crest and decreases in the troughs. The variance is observed to be discontinuous in between the fourth and fifth streamwise region. The mean elevation is continuous between these regions and the source of the discrepancy in the variance is believed to be an increased noise level in the data for the fifth region. (The video images for this region in this case were slightly lower in contrast, due to lower power in the laser sheet used for illumination. This is most likely due to drift in the alignment of the mirrors in the laser cavity.)

Figure 5 shows the results for an angle of attack of 6° . This resulted in the maximum level of dissipation (97%). Figure 5a shows samples of the instantaneous surface elevation profiles for the five streamwise regions. The breaking wave crest has 'flattened' somewhat and is centred at $x = 1.10$ m. The region of strong surface activity now begins about 0.20 m ahead of the wave crest (27% of the wavelength) and, again, extends a similar distance downstream of the crest. Figure 5b shows profiles of the temporal mean of the surface elevation and slope for this case. The beginning of the breaking region has moved forward to roughly the trough of the wave. The ampli-

tude of the following wave is 62% smaller than for the 3° angle-of-attack case, and 44% smaller than that for 4°. Figure 5c shows the variance of the surface elevation for the five streamwise regions. Ahead of the breaking region, the variance is at the noise level for the surface elevation measurements. A local maximum in the variance, $5.9 \times 10^{-5} \text{ m}^2$, occurs near the ‘toe’ of the breaking wave, but there is a second local maximum of $7.0 \times 10^{-5} \text{ m}^2$ closer to the wave crest. The variance decreases rapidly downstream to a level of $6.2 \times 10^{-6} \text{ m}^2$ for distances larger than 0.26 m downstream of the breaking crest (37% of the following wavelength). Further downstream, there is a general downward trend which may be due to dissipation of the small-scale surface disturbances by the turbulence generated by the breaking. There is again a slight increase in the variance near the second crest and decreases in the troughs.

(ii) *Wavenumber spectra and spatial covariance*

For the purpose of comparing with the radar measurements, the surface elevation measurements obtained from each video frame, as discussed in § 2*b* (ii), were divided into two 256-element (approximately 0.20 m) segments. The unbiased discrete spatial covariance function, given by

$$C(x_m) = \frac{1}{256 - m} \sum_{n=0}^{255-m} \eta(x_n)\eta(x_n + x_m), \quad m = 0, 1, \dots, 255, \quad (3.7)$$

was computed for each of these segments and averaged over the set of 256 frames collected at each location. For large x_m , these estimates become less reliable because a small number of data points are used in the computation. Therefore, the covariance functions were weighted by a Hanning window with a width of 0.25 m. This acted to reduce the variance in the spectral estimates discussed later while also reducing the bias which exists in spectral estimates calculated using the Blackman–Tukey method (Proakis & Manolakis 1992). Examples of these covariance functions are shown in figure 6.

The two-dimensional wavenumber spectra were estimated using

$$S(k_x, k_y) = \frac{1}{4\pi^2} \iint C(x, y) e^{i(k_x x + k_y y)} dx dy, \quad (3.8)$$

where $C(x, y)$ is the two-dimensional height covariance function, obtained from the one-dimensional functions discussed previously by assuming a uniform angular distribution. By fitting (in a least-squares sense) a 20th-order polynomial to the one-dimensional covariance functions, the two-dimensional covariance functions were re-sampled onto a rectangular grid which allowed equation (3.8) to be evaluated using a two-dimensional fast Fourier transform.

Examples of the resulting height spectra are shown in figure 7. Figure 7*a* illustrates the changes in the observed spectra with distance behind the breaking crest for a given foil angle. The wave spectra downstream from the breaking crest are shifted to the left due to interactions with the diverging surface current in this region, as discussed above. Beyond the third window, the spectra remain relatively constant, with presumably a slow decay due to viscosity and turbulence.

The changes in the wave spectra at the breaking crest with increasing energy dissipation (as determined by the foil angle setting) are shown in figure 7*b*. Although the total height variance continues to increase, the spectral density at wavenumbers larger than 100 rad m^{-1} appears to ‘saturate’ at a value of approximately $ak^{-3.5}$ with $a = 0.003 \text{ m}^{1/2}$.

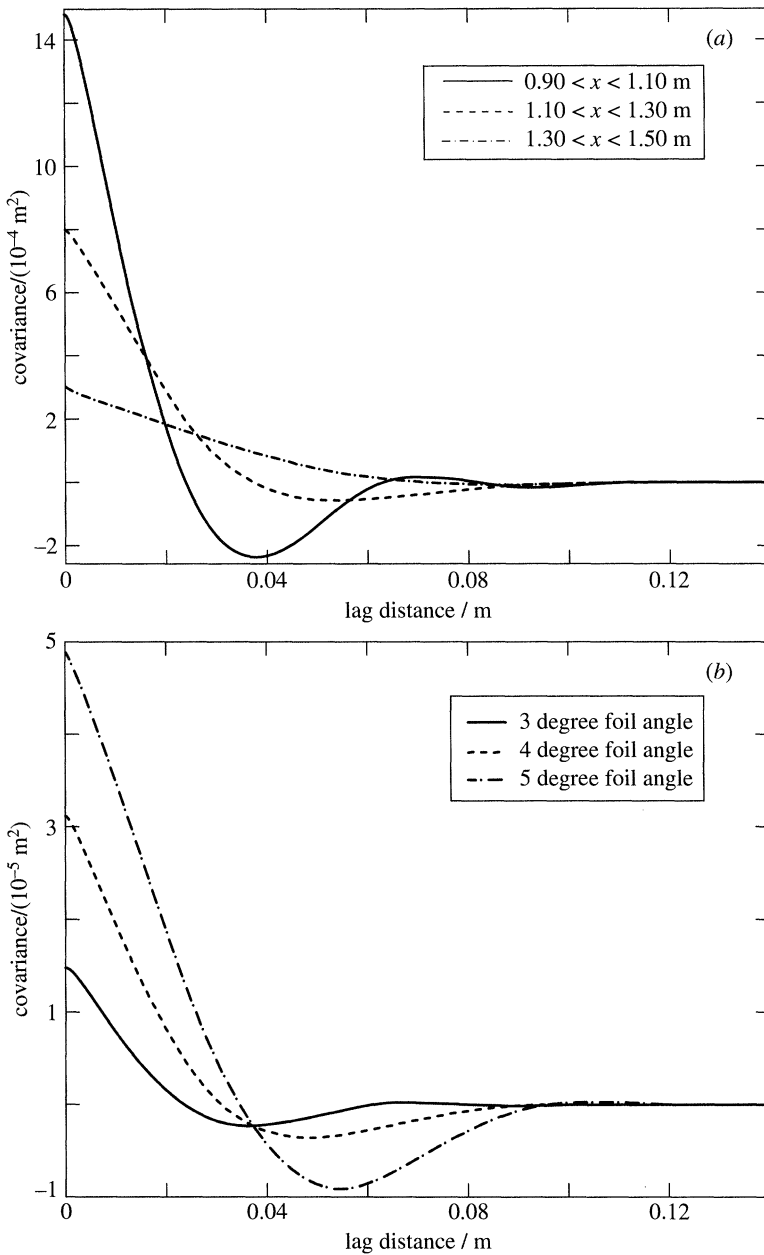


Figure 6. Covariance function for (a) the forward face of the breaking crest, and two downstream locations for $\alpha = 3^\circ$: —, $0.90 < x < 1.10 \text{ m}$; ---, $1.10 < x < 1.30 \text{ m}$; - · - · -, $1.30 < x < 1.50 \text{ m}$; and (b) the forward face of the breaking crest for varying angles of attack: —, $\alpha = 3^\circ$; ---, $\alpha = 4^\circ$; - · - · -, $\alpha = 6^\circ$.

The assumption of a uniform angular distribution causes some error in these spectral estimates, but this error is believed to be smaller than about a factor of two, at least for the wavelengths that influence the radar backscatter calculations described below. This conclusion is based on measurements of the two-dimensional slope spectrum at selected locations, which showed a nearly isotropic distribution

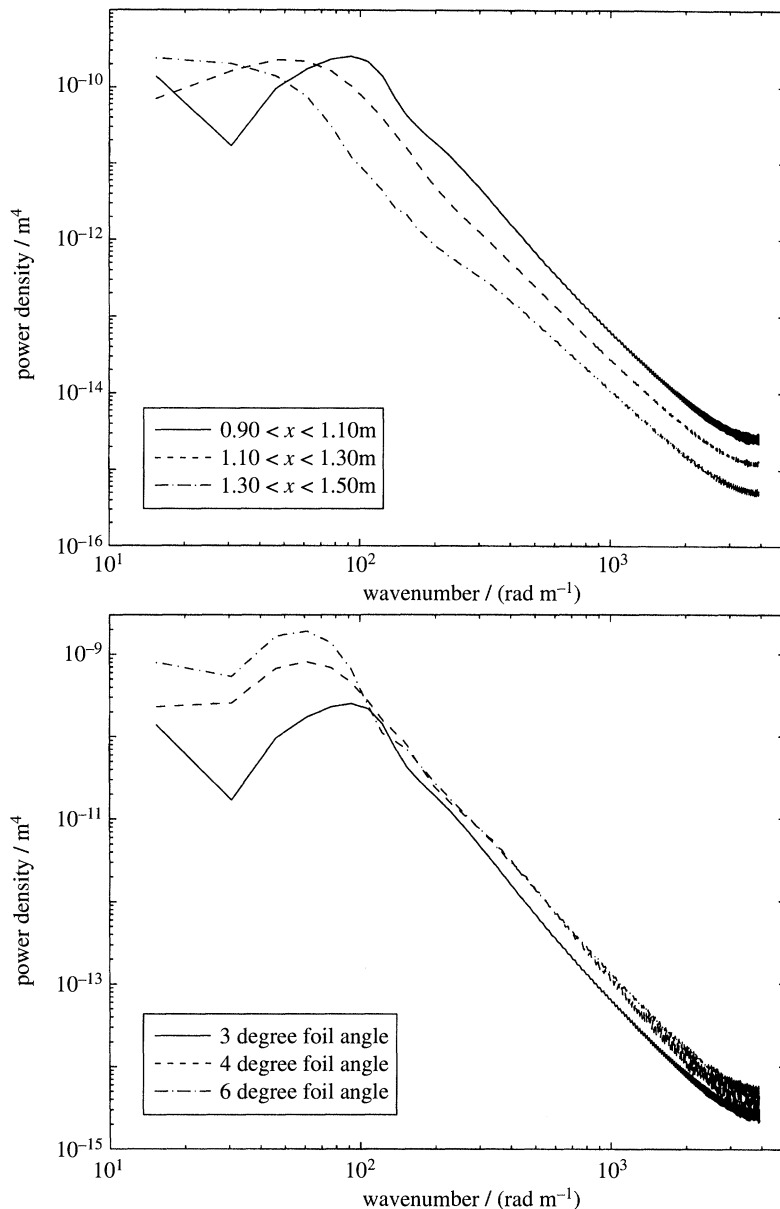


Figure 7. Wavenumber (k_x) spectrum for (a) the forward face of the breaking crest, and two downstream locations for $\alpha = 3^\circ$: —, $0.90 < x < 1.10\text{ m}$; ---, $1.10 < x < 1.30\text{ m}$; - · - · -, $1.30 < x < 1.50\text{ m}$; and (b) the forward face of the breaking crest for varying angles of attack: —, $\alpha = 3^\circ$; ---, $\alpha = 4^\circ$; - · - · -, $\alpha = 6^\circ$.

for wavelengths shorter than about 2 cm (Wolf 1994). Banner & Fooks (1985) calculated the lateral and longitudinal coherence of the frequency spectra measured by two wave probes for an experimental arrangement similar to ours, and found significant differences in the shapes of the coherence functions at long lags. However, their coherence functions tended to be fairly similar at short lags, having equivalent Gaussian widths on the order of 1–2 cm in the longitudinal direction and 0.5–2 cm in

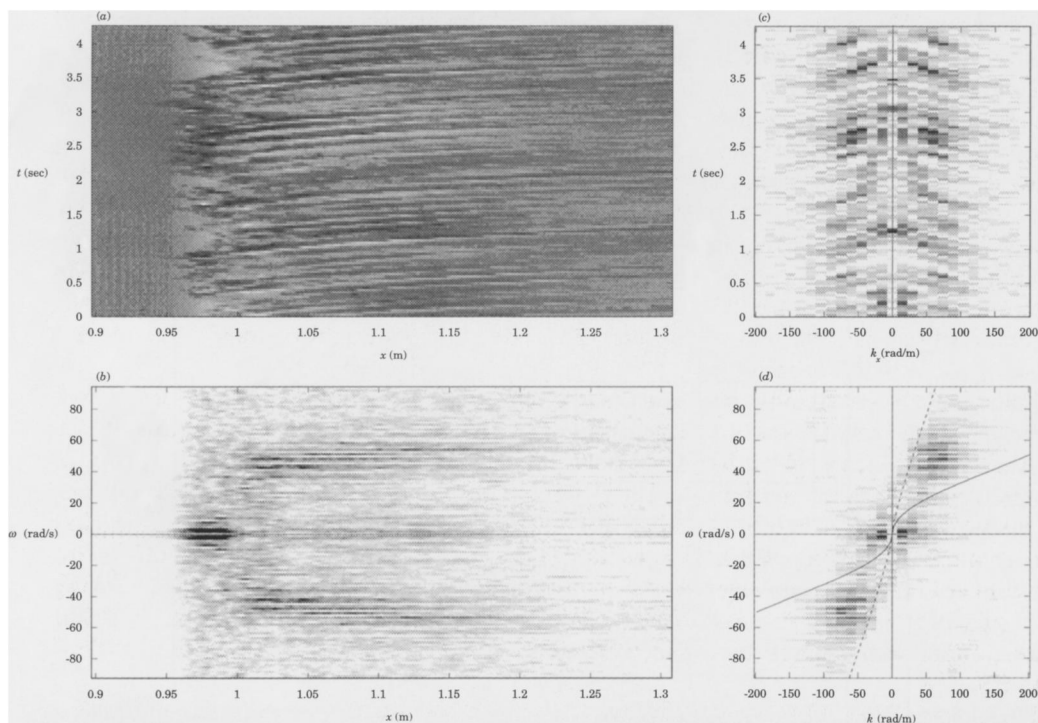


Figure 8. Results for the breaking crest region of the wave for $\alpha = 3^\circ$: (a) instantaneous surface elevation profiles $\eta(x, t) - \bar{\eta}(x)$; (b) spatial variation of the frequency spectrum; (c) temporal variation of the streamwise wavenumber spectrum; (d) wavenumber-frequency spectrum. Dispersion relation for downstream propagating (+x) waves for: —, stationary fluid, $U = 0$; - - -, fluid velocity of $U = 1.08 \text{ m s}^{-1}$.

the lateral direction. The effect of such an asymmetry can be estimated by assuming that the surface height covariance function has the same shape in both directions but is compressed in the lateral direction by the factor a , i.e. $C(x, y) = C_i(x, ay)$, where $c_i(x, y)$ is the isotropic covariance function. The spectrum corresponding to this 'compressed' covariance function is then $S(k_x, k_y) = (1/a)S_i(k_x, k_y/a)$, so along the k_x -axis the spectrum is merely reduced by the factor $1/a$. If we interpret the measurements of Banner & Fooks (1985) as indicating that $1 < a < 2$, then the spectra calculated under the isotropic assumption overestimate the actual spectra by at most a factor of two.

(iii) Spacetime behaviour in the breaking-wave crest

The elevated variance which occurs in the region of the breaking wave crest gives rise to a large radar cross-section. The radar backscatter results are discussed below. Here we will examine the crest region of the 3° angle-of-attack wave to attempt to learn more about the nature of the disturbances in this region. We will do this by looking at the spacetime behaviour of the surface elevation profiles in this region. While the results presented here will be only for the 3° angle-of-attack wave, they are similar in most respects to those of the other cases.

Figure 8 shows the behaviour of the surface disturbances in the crest region of the gentlest breaking wave. Figure 8a shows the fluctuating surface elevation ($\eta - \bar{\eta}$) as a function of streamwise position x and time t . Darker regions in the plot correspond to

positive (upward) fluctuations and lighter regions correspond to negative (downward) fluctuations. Upstream of the breaking region there are no surface disturbances and so the grey level there corresponds to zero. The surging 'toe' region of the breaker is clearly evident in this image at the streamwise location corresponding to the maximum in the variance shown in figure 3*c*. Just downstream of the toe, there are disturbances which clearly travel downstream as time progresses. The amplitude of these disturbances decreases as they move downstream. Figure 8*b* shows the two-sided frequency (ω) spectrum versus streamwise position for the image shown in figure 8*a*. The surging in the toe region is clearly associated with low-frequency disturbances (roughly 2.95 rad s^{-1}). The downstream travelling disturbances identified in figure 8*a* are centred at a frequency of roughly 50 rad s^{-1} , and appear to be unrelated to the disturbances at the toe. The amplitude of the disturbances again appears to decrease in the downstream direction.

The range of streamwise positions where these moving waves occur runs from just forward of the crest to where the mean surface elevation is roughly equal to the spatial-mean surface elevation for the following wave. In the laboratory reference frame, the velocity of the fluid at the former location is near zero, while that at the latter location it is roughly equal to that of the underlying flow (U_0). The fact that the apparent frequency remains constant over the range of streamwise positions for the downstream propagating waves is consistent with the idea of waves propagating on a spatially varying current. While the apparent frequency remains constant, the wavenumber will change to reflect the effect of the spatial variations in the fluid velocity.

Figure 8*c* shows the one-dimensional wavenumber (k_x) spectrum as a function of time. Clearly visible in the figure are the trends toward lower wavenumber with increasing time. As the waves propagate downstream from a region of low velocity to a region of high velocity, the wavelength increases (wavenumber decreases). This is consistent with the other observed behaviours.

Figure 8*d* shows the wavenumber–frequency (k_x – ω) spectrum. The low-frequency disturbances in the toe region are seen to be also associated with low wavenumbers. The higher-frequency disturbances associated with the downstream propagating waves show up as discrete frequencies, but each is associated with a range of wavenumbers. This is due to the increase in wavelength caused by the increase in fluid velocity in the downstream direction. In figure 8*d*, the second and fourth quadrants are associated with waves which propagate upstream (in the $-x$ -direction), while the first and third quadrants are associated with downstream propagating waves. The disturbances associated with the downstream propagating waves are clearly in the expected quadrants, while those associated with the toe region reside in all four quadrants. For a given fluid velocity U , the linear dispersion relation is given by

$$\omega = (gk + Tk^3)^{1/2} + Uk_x, \quad (3.9)$$

where k is the magnitude of the wave vector (see, for example, Crapper 1984). Two such lines are shown in figure 8*d* for $k = k_x$. The dashed line is the dispersion relation for $U = 1.08 \text{ m s}^{-1}$, the underlying flow velocity in the channel. The value of U at the downstream end of the breaking crest region ($x \approx 1.30 \text{ m}$) should be close to this. The solid line is for $U = 0$, representative of the relatively stagnant fluid in the breaking region ahead of the wave crest (see Lin & Rockwell 1994). For waves propagating from the stagnant region ahead of the crest to the higher velocity region behind, the solid line and the dashed line should 'bracket' the range of wavenumbers observed, as is shown in the figure.

The changes in the wave amplitude due to the spatially varying surface current in the region behind the wave crest can be estimated using conservation of wave action. The wave-action spectral density is defined as $N(k_x, k_y) = \rho c(k) S(k_x, k_y)$, where $S(k_x, k_y)$ is the height spectral density and $c(k)$ is the phase velocity (see Apel 1987). For the case in question, conservation of wave action reduces to $N = \text{const.}$ along ray paths defined by $\omega = \text{const.}$ (where ω is the apparent frequency given in equation (3.9)). Using the estimates of the wavenumber spectrum described in §3c(ii), the action spectrum was calculated for the region $0.90 < x < 1.10$ m. In this region, the velocity U is small, and was taken to be zero. The resulting action spectrum was mapped onto the corresponding set of wavenumbers for the downstream location where $U = 1.08 \text{ m s}^{-1}$ using (3.9) with $\omega = \text{const.}$ The height spectrum corresponding to $U = 1.08 \text{ m s}^{-1}$ was then determined from the action spectrum, and was integrated to find the height variance at this location. The change in the height variance computed by this procedure was found to be 94%, which is comparable to the observed change of 90% between the location of the peak in the variance and $x = 1.30$ m. This indicates that wave-current interactions are likely to be responsible for the observed change in roughness downstream of the breaking crest.

(d) Radar backscatter measurements

Plots of the measured radar cross-section per unit area (RCS) versus distance are shown in figures 3–5*d* and *e* for each of the foil angle settings. These plots indicate that the maximum radar cross-section occurs near the crest of the breaking wave for the upwave look direction (figures 3–5*e*), and is approximately the same (–3 dB) for both polarizations and for all three foil angles. The location of the maximum RCS shifts forward slightly as the foil angle is increased, as does the point of maximum mean slope and maximum roughness. However, the maximum RCS occurs behind the point of maximum mean slope in all three cases.

These maximum RCS values are roughly consistent with those observed in the Chesapeake Bay by Jessup *et al.* (1991*a*). The fact that the maximum RCS does not occur at the location of maximum slope is inconsistent with the hypothesis of Loewen & Melville (1991) regarding the role of specular scattering in their laboratory experiments. This inconsistency, however, may be due to the inherent difference between stationary and transient breakers.

For the downwave look direction (figures 3–5*d*), the maximum RCS is slightly smaller (about –6 dB) but is again almost the same for both polarizations and for all three foil angles, although the vv returns are slightly higher than the hh returns at the lower foil angle settings.

Downstream from the breaking crest, the RCS falls off rapidly and the difference between the vv and hh returns becomes larger, reaching a maximum of about 5–7 dB in the region between the two wave crests where the RCS is at a minimum. A noticeable increase in RCS occurs near the second wave crest, at least for the smaller foil angles. This increase is larger for hh than for vv polarization. As the foil angle is increased, the maximum RCS value at the second crest remains about the same, but the minimum value between the two crests increases.

(e) Radar backscatter modelling

In order to gain further insight into the radar backscatter observations, we used the surface measurements described in the previous sections as inputs into the Bragg

scattering model, a recent derivation and exposition of which has been given by Plant (1990). According to this model, the radar cross-section per unit area for a look direction in the x - z plane is given by

$$\sigma^0 = 8\pi k_e^4 |g_{ij}(\theta)|^2 \{S(k_B, 0) + S(-k_B, 0)\}, \quad (3.10)$$

where k_e is the electromagnetic wavenumber, $k_B = 2k_e \sin \theta$ is the Bragg wavenumber, $S(k_x, k_y)$ is the two-dimensional wave-height spectrum, θ is the incidence angle and

$$g_{VV} = \frac{[\epsilon + (\epsilon - 1) \sin^2 \theta](\epsilon - 1) \cos^2 \theta}{[\epsilon \cos \theta + \sqrt{\epsilon - \sin^2 \theta}]^2} \quad (3.11)$$

for vertical polarization and

$$g_{HH} = \frac{(\epsilon - 1) \cos^2 \theta}{[\cos \theta + \sqrt{\epsilon - \sin^2 \theta}]^2} \quad (3.12)$$

for horizontal polarization, where $\epsilon = 60 - i35$ is the relative dielectric constant of the medium (water) as calculated from the Debye equation for a water temperature of 20 °C (Ulaby *et al.* 1986).

For the nominal incidence angle of 45°, the Bragg wavenumber is 310 rad m⁻¹, which corresponds to a wavelength of 0.020 m. The spectral density at this wavenumber was extracted from each of the elevation spectra described in § 3c(ii), and these spectral densities were used to calculate the radar cross-section per unit area within each 0.20 m subwindow. These σ^0 values were then weighted by the antenna gain pattern (shown in figure 2) in order to obtain the predicted RCS for each antenna position. These predictions are shown in figure 9. Note that this model predicts only a very small upwave-downwave difference, and the ratio of HH to VV backscatter is almost constant, since it does not take into account the slope of the underlying long-wave surface. (The slight differences in the upwave and downwave RCS values and the variations in the polarization ratio are due to differences between the antenna gain patterns at the water surface for the different look directions and polarizations.)

Although these simple-Bragg-model predictions bear some qualitative similarities to the observations, there are significant differences between the predicted and observed RCS values, ranging from about a 10 dB underprediction of the HH return at the breaking wave crest (for the 3° upwave case) to a 3 dB overprediction of the VV return in the trough region for the 6° upwave and downwave cases. Note also that this model also fails to explain the observed backscatter peak in the region of the second wave crest.

The performance of the Bragg model can be improved by computing the local incidence angle at each point on the surface, and using this local incidence angle to compute both the Bragg wavelength and the coefficients g_{HH} and g_{VV} in the Bragg model. We will refer to this modification as the 'tilted-Bragg' model. For our measurements, the local incidence angle also changes within the footprint of the antenna due to the nearness of the antenna to the surface, and this effect was taken into account along with the changes due to the local temporal mean surface slope. The radar cross-section per unit area was calculated for each location in the surface elevation profiles, using the elevation spectrum for the 0.20 m subwindow in which the point under consideration was located. Contributions from locations at which the local incidence angle was less than 13.6° (which would imply a Bragg wavenumber less than $\frac{1}{3}k_B$, where $k_B = 310$ rad m⁻¹ is the nominal Bragg wavenumber) were excluded from

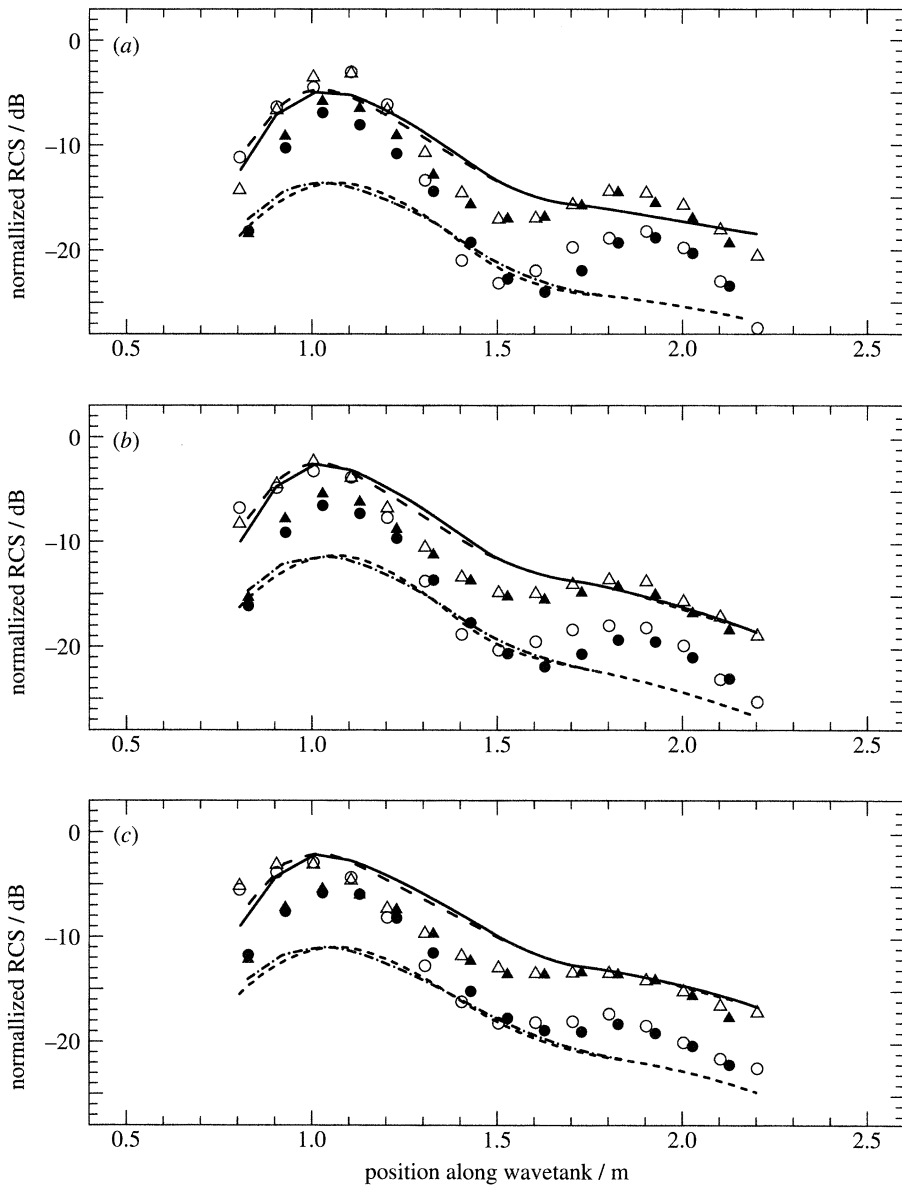


Figure 9. Comparison of measured radar cross-section and predictions from the simple Bragg-scattering model for: (a) $\alpha = 3^\circ$; (b) $\alpha = 4^\circ$; (c) $\alpha = 6^\circ$. For downwave look direction: - - - - \bullet , HH; - - - \blacktriangle , VV; for upwave look direction: - - - \circ , HH; — \triangle , VV. Symbols represent experimental measurements; lines represent model predictions.

the calculation. These values were then weighted by the antenna gain pattern and integrated to obtain the predicted RCS corresponding to each measurement location. The results of these calculations are shown in figure 10.

The tilted Bragg model yields better agreement with the measurements, particularly in the region of the second wave crest, than the simple Bragg model. The agreement is especially encouraging in view of the fact that no arbitrary scale factors were applied to the measurements or the model predictions. (As discussed in

Proc. R. Soc. Lond. A (1996)

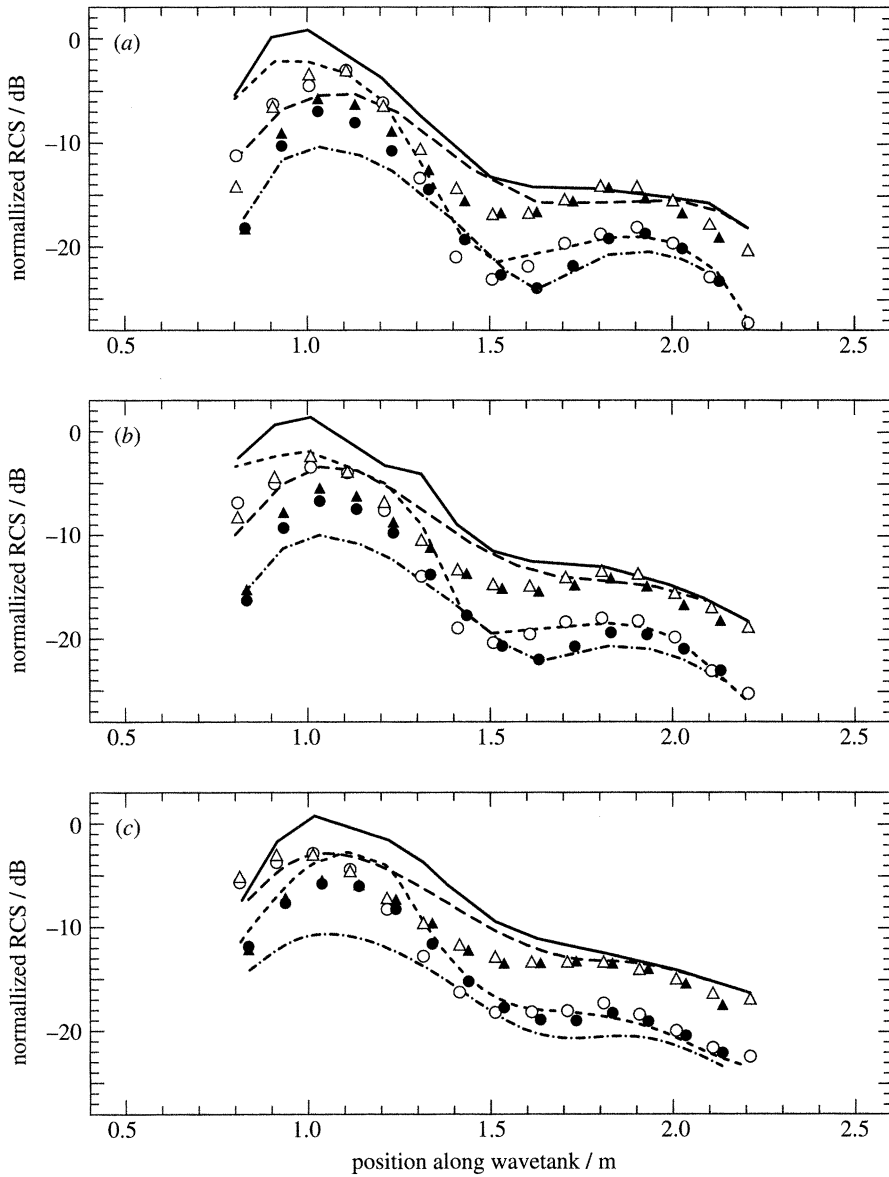


Figure 10. Comparison of measured radar cross-section and predictions from the tilted Bragg-scattering model for: (a) $\alpha = 3^\circ$; (b) $\alpha = 4^\circ$; (c) $\alpha = 6^\circ$. For downwave look direction: - - - - \bullet , HH; - - - \blacktriangle , VV; for upwave look direction: - - - \circ , HH; — \triangle , VV. Symbols represent experimental measurements; lines represent model predictions.

§ 3 c (ii), the assumption of an isotropic spatial covariance may cause the spectral density for $k_y = 0$ be overestimated by as much as a factor of two. This translates into a possible 3 dB overprediction of the RCS.) While the agreement is generally good, the tilted Bragg model clearly fails to reproduce some important trends in the data, such as the tendency for both the upwave-downwave and the VV-HH backscatter ratios to diminish in the region near the breaking crest.

In order to gain some insight into the reasons for these discrepancies, we have

plotted the ratio of the predicted to the observed RCS versus the parameter

$$\xi = 4k_e^2 \langle \eta_s^2 \rangle \cos^2 \theta, \quad (3.13)$$

where $\langle \eta_s^2 \rangle$ is the height variance associated with wavenumbers greater than $\frac{1}{3}k_B$, where k_B is again the nominal Bragg wavenumber. This parameter is formally required to be much less than unity for the small perturbation method to be valid (Brown 1978). The results shown in figure 11 indicate that this criterion is not met for a large number of our observations, and that the error in the prediction increases with this parameter. For vv polarization, the error is (almost) always positive for large ξ , indicating an overprediction by the Bragg model, while for hh polarization the error is mostly positive for upwave look directions and negative for downwave look directions. The overpredictions may be due to a 'saturation' effect, which must occur eventually since the reflectivity cannot increase indefinitely with increasing roughness, as predicted by the Bragg model. On the other hand, the underprediction of the downwave hh returns appears to be associated with a breakdown in the Bragg model at the large local incidence angles which occur on the forward face of the breaking crest for the downwave look direction.

It is interesting to note that the inclusion of a specular scattering component would not improve the comparison, since it would add a larger contribution in the upwave than in the downwave direction, and the calculated upwave RCS is already too large at the breaking crest. However, specular scattering is not expected to contribute significantly anyway, because of the reduction of this component by diffraction effects associated with the small-scale roughness on the forward face of the wave. Thompson (1988) has presented a derivation of the two-scale model which shows that the specular component should be multiplied by the factor $(1 - \xi)$, where ξ is the small-scale roughness parameter given by (3.13), which is assumed in the derivation to be much smaller than one. In our case, this parameter is larger than unity on the forward face of the breaking crest, and so the derivation is not strictly valid, but it does indicate that the specular component would be expected to be greatly reduced by the presence of this roughness.

4. Summary and conclusions

In this study, we examined stationary breaking waves generated by a hydrofoil in a moving stream. The level of energy dissipation due to breaking was varied by changing the foil angle of attack α from 3° to 6° . Time series of surface elevation profiles were obtained for the breaking crest region and the following waves. We also measured the X-band radar backscatter from these breaking waves, at an incidence angle of 45° , for both hh and vv polarizations and with the radar looking both upwave and downwave. These results were compared to model predictions using the surface elevation information as input.

Dissipation levels for these stationary breaking waves ranged from 62% to 97%. These levels of dissipation corresponded to equivalent prebreaking steepnesses of 0.33 and larger. At small angles of attack, the dissipation levels are consistent with those observed by Rapp & Melville (1990) and Ramberg & Griffin (1987) for non-stationary propagating waves.

The breaking crest region of the waves exhibits large surface disturbances and has the largest radar cross-section. Large low-frequency disturbances occur in the 'toe' region, and the maximum variance in the surface elevation generally occurs at

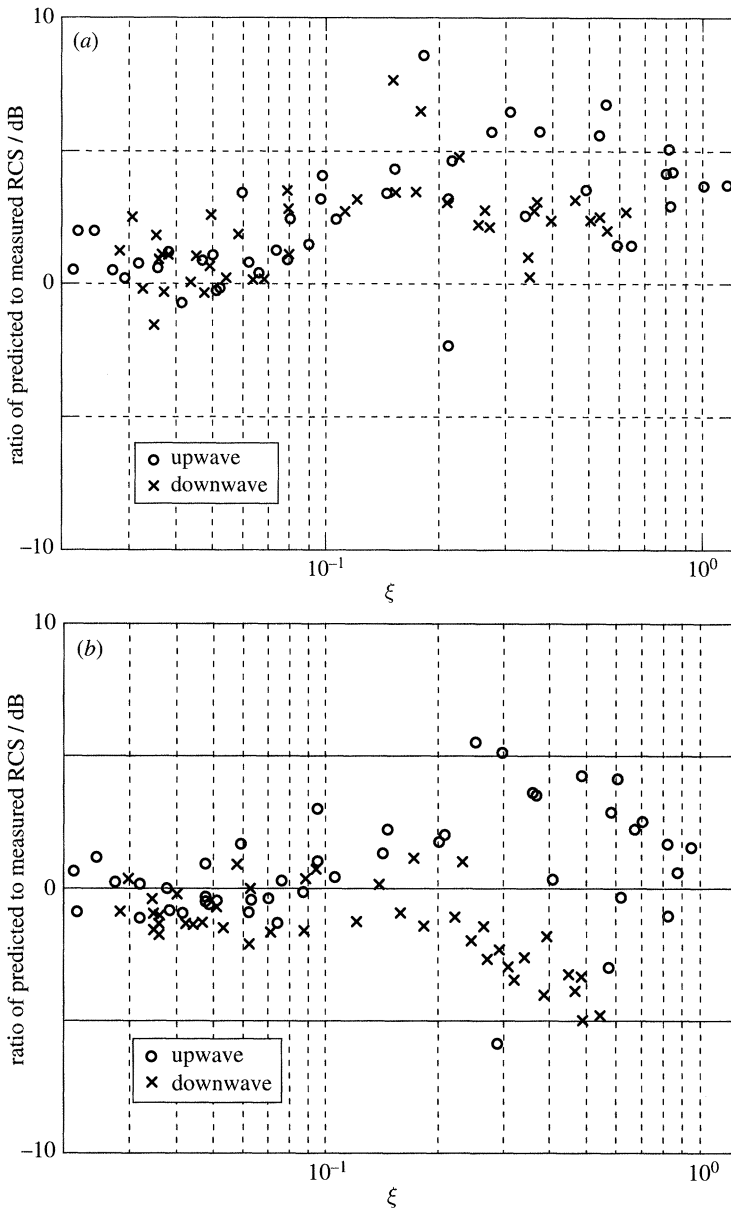


Figure 11. Ratio of measured to predicted radar cross-section for the tilted Bragg- scattering model versus surface-roughness parameter ξ for upwave and downwave looking observations: (a) VV polarization; (b) HH polarization.

this location. Downstream-moving waves appear just ahead of the crest and, due primarily to interaction with the spatially varying current set up by the stationary wave, decrease in amplitude by an order of magnitude as they propagate downstream. These surface disturbances remain at a low level thereafter, but are steepened slightly near the crests of the following waves, most likely due to the converging flow under the crests. For the most violent breaking wave $\alpha = 6^\circ$, the variance of the surface elevation decreased monotonically downstream, indicating dissipation of wave energy

Proc. R. Soc. Lond. A (1996)

due to subsurface turbulence generated in the breaking region can be significant. Also for $\alpha = 6^\circ$, the disturbances in the toe and crest regions of the breaker result in two distinct maxima in the surface-elevation variance.

The maximum radar cross-section per unit area observed near the breaking crest was on the order of 0.5 (-3 dB) in the upwave look direction and 0.25 (-6 dB) in the downwave look direction, for both HH and VV polarization. Behind the breaking crest, the radar cross-section decreased rapidly and then levelled off or increased slightly in the region of the second wave crest, and an increasing difference between the VV and HH backscatter was observed as the overall backscatter level decreased.

The measured surface statistics were used as inputs into the Bragg scattering model to calculate the expected radar backscatter, and these calculations were compared with the measured radar cross-sections. Although the variations in the observed radar cross-section downstream from the breaking crest are satisfactorily explained by the Bragg model when surface tilt effects are taken into account, the backscatter from the breaking crest itself is less well predicted. The VV-polarization returns are overpredicted for both upwave and downwave look directions, while the HH returns are generally overpredicted for the upwave look direction and underpredicted for the downwave look direction. As a result, the HH-to-VV polarization ratio at the breaking crest (which is near unity for both look directions) is fairly well predicted for the upwave look direction but is underpredicted by up to 10 dB for the downwave look direction. This breakdown is to be expected, since the small-scale height variations in the breaking region exceed the criterion for the validity of the small perturbation method which is used to derive the Bragg model. Specular scattering is not expected to contribute significantly to the observed RCS variations, because of diffraction effects caused by the small-scale roughness on the forward face of the breaking crest.

The breaking waves studied in this laboratory investigation are of course not the same as those in the open ocean. Breaking waves on the open ocean, being transient, are expected to go through several stages of development including a prebreaking phase during which the forward face may be steeper and the crest is sharper than in the cases we investigated. During this phase, specular reflection or edge diffraction effects may be important for some incidence angles and for upwave look directions. Just after breaking, the wave surface may more closely approximate the shapes encountered in our experiments, although if the wind speed is sufficiently high other effects which we have not investigated will certainly be present as well. Perhaps the situation in which our results are most directly applicable would be the case in which waves are steepened by interactions with variable surface currents such as in ocean fronts or internal waves (see, for example, Lyzenga 1991) under low wind conditions. Even in this case, it is still an open question as to which stage of breaking produces the largest backscatter. However, for look directions other than upwave, it seems likely that the dominant mechanism would have to be scattering from the small-scale roughness generated by the breaking process.

The contribution of wave breaking to the average backscatter from the ocean surface depends on considerations which are beyond the scope of this study, such as the size and frequency of occurrence of breaking crests. It is possible that these quantities could be estimated from other statistical descriptions such as the wave-height spectrum. Alternatively, it may be possible to establish a link to open ocean conditions via energy dissipation considerations. However, the fact that the radar cross-section per unit area that we observed in the region of the breaking wave crests

is 1–2 orders of magnitude larger than mean oceanic backscatter levels would appear to reaffirm the significance of this phenomenon, even at intermediate incidence angles.

The extrapolation of our results to other radar frequencies and incidence angles and to other breaking wavelengths is also beyond the scope of this paper, although the surface measurements presented here should allow at least some extrapolations if used in conjunction with an appropriate set of backscatter calculations. The Bragg model can be used for crude estimates but does not give accurate results for the backscatter from the breaking crest region. Most of the short-wave energy generated by breaking is confined to a region extending roughly $\frac{1}{2}$ – $\frac{1}{4}$ wavelength in the direction of propagation of the breaking wave. However, significant amounts of wave energy at slightly longer wavelengths escape from this region and are in fact enhanced by the wave-current interaction process (near the second crest). Therefore, we might expect the breaking wave backscatter at lower radar frequencies to be less localized but more persistent than at X-band.

This work was funded by the Office of Naval Research–Ocean, Atmosphere and Space Science and Technology Department, Sensing and Systems Division, under University Research Initiative Grant Number N00014-92-J-1650, monitored by Dr D. Trizna and Dr F. Herr. The construction of the water channel facility used for these experiments was supported by the University of Michigan and the Department of Naval Architecture & Marine Engineering, as well as the Fluid Dynamics Program of ONR under Contract No. N00014-86-K-0684, monitored by Dr E. P. Rood. This support is gratefully acknowledged. Acknowledgment is also due to R. G. Donaldson, J. Krasny, G. Opas, Denise Jones and W. Kirkpatrick, whose various skills led to the successful construction of the water channel facility, and to D. Kraemer for the initial qualification measurements. Thanks also to E. Dano, for help in performing the radar calibration measurements, and to Kevin Mitchell of Michigan Wheel Corp. for help in both selecting and procuring the propeller for the channel.

References

- Apel, J. R. 1987 *Principles of ocean physics*, pp. 481–482. New York: Academic.
- Balanis, C. A. 1982 *Antenna theory: analysis and design*. New York: Wiley.
- Banner, M. L. & Fooks, E. H. 1985 On the microwave reflectivity of small-scale breaking water waves. *Proc. R. Soc. Lond. A* **399**, 93–109.
- Bradshaw, P. & Pankhurst, R. C. 1964 The design of low-speed wind tunnels. *Prog. Aero. Sci.* **5**, 1–69.
- Brown, R. B. 1978 Backscattering from a Gaussian-distributed, perfectly conducting rough surface. *IEEE Trans. Antenna Propagat.* **AP-26**, 472–482.
- Crapper, G. D. 1984 *Introduction to water waves*. New York: Ellis Horwood.
- Duncan, J. 1981 An experimental investigation of breaking waves produced by a towed hydrofoil. *Proc. R. Soc. Lond. A* **377**, 331–348.
- Duncan, J. 1983a The breaking and non-breaking wave resistance of a two-dimensional hydrofoil. *J. Fluid Mech.* **126**, 507–520.
- Duncan, J. 1983b A note on the evaluation of the wave resistance of two-dimensional bodies from measurements of the downstream wave profile. *J. Ship Res.* **27**, 90–92.
- Duncan, J. 1993 Surface roughness in the wake of a steady breaking wave. *Proc. 3rd Int. Offshore and Polar Engng Conf., ISOPE*, pp. 39–44.
- Ebuchi, N., Kawamura, H. & Toba, Y. 1993 Physical processes of microwave backscattering from laboratory wind wave surfaces. *J. Geophys. Res.* **98**, 14 669–14 681.
- Hasselmann, K., Raney, R. K., Plant, W. J., Alpers, W., Schuchman, R. A., Lyzenga, D. R., Rufenach, C. L. & Tucker, M. J. 1985 Theory of synthetic-aperture radar ocean imaging: A MARSEN view. *J. Geophys. Res.* **90**, 4659–4686.
- Jessup, A. T., Keller, W. C. & Melville, W. K. 1990 Measurement of sea spikes in microwave backscatter at moderate incidence. *J. Geophys. Res.* **95**, 9679–9688.
- Proc. R. Soc. Lond. A* (1996)

- Jessup, A. T., Melville, W. K. & Keller, W. C. 1991*a* Breaking waves affecting microwave backscatter: 1. Detection and verification. *J. Geophys. Res.* **96**, 20 547–20 559.
- Jessup, A. T., Melville, W. K. & Keller, W. C. 1991*b* Breaking waves affecting microwave backscatter: 2. Dependence on wind and wave conditions. *J. Geophys. Res.* **96**, 20 561–20 569.
- Lewis, B. L. & Olin, I. D. 1980 Experimental study and theoretical model of high-resolution radar backscatter from the sea. *Radio Sci.* **15**, 815–828.
- Lin, J.-C. & Rockwell, D. 1994 Instantaneous structure of a breaking wave. *Physics Fluids* **6**, 2877–2879.
- Loehrke, R. I. & Nagib, H. M. 1972 AGARD Report No. 598. Experiments on management of free-stream turbulence. AGARD-NATO.
- Loewen, M. R. & Melville, W. K. 1991 Microwave backscatter and acoustic radiation from breaking waves. *J. Fluid Mech.* **224**, 601–623.
- Longuet-Higgins, M. S. 1974 Integral properties of periodic gravity waves of finite amplitude. *Proc. R. Soc. Lond. A* **342**, 157–175.
- Lyzenga, D. R. 1991 Interaction of short surface and electromagnetic waves with ocean fronts. *J. Geophys. Res.* **96**, 10 765–10 772.
- Melville, W. K. & Rapp, R. J. 1985 Momentum flux in breaking waves. *Nature* **317**, 514–516.
- Melville, W. K., Loewen, M. R., Felizardo, F. C., Jessup, A. T. & Buckingham, M. J. 1988 Acoustic and microwave signature of breaking waves. *Nature* **336**, 54–59.
- Phillips, O. M. 1988 Radar returns from the sea surface—Bragg scattering and breaking waves. *J. Phys. Oceanogr.* **18**, 1065–1074.
- Plant, W. J. 1990 Bragg scattering of electromagnetic waves from the air/sea interface. In *Surface waves and fluxes* (ed. G. L. Geernaert & W. J. Plant). Dordrecht: Kluwer.
- Proakis, J. G. & Manolakis, D. G. 1992 *Digital signal processing principles, algorithms and applications*, ch. 12. New York: Macmillan.
- Ramberg, S. E. & Griffin, O. M. 1994 Laboratory study of steep and breaking deep-water waves. *J. Waterway, Port, Coastal & Ocean Engng* **113**, 493–506.
- Rapp, R. J. & Melville, W. K. 1990 Laboratory measurements of deep-water breaking waves. *Phil. Trans. R. Soc. Lond. A* **331**, 735–800.
- Thompson, D. R. 1988 Calculation of radar backscatter modulations from internal waves. *J. Geophys. Res.* **93**, 12 371–12 380.
- Trizna, D. B., Hansen, J. P., Huang, P. & Wu, J. 1993 Ultra-wideband radar studies of steep-crested waves with scanning laser measurements of wave slope profiles. *Dyn. Atmos. Oceans* **20**, 33–53.
- Trizna, D. B., Hansen, J. P., Huang, P. & Wu, J. 1991 Laboratory studies of radar sea spikes at low grazing angles. *J. Geophys. Res.* **96**, 12 529–12 537.
- Ulaby, F. T., Moore, R. K. & Fung, A. K. 1986 *Microwave remote sensing—active and passive*, vol. III. Reading, MA: Addison-Wesley.
- Whitehead, L. G., Wu, L. Y. & Waters, M. H. L. 1951 Contracting ducts of finite length. *Aero. Q.* **2**, 254–271.
- Wolf, C. 1994 Surface properties of breaking water waves. Diploma thesis, University of Heidelberg.

Received 13 February 1995; revised 23 May 1995; accepted 27 June 1995